Comparison of SeaWinds Backscatter Imaging Algorithms

David G. Long, *Fellow, IEEE*

***Abstract*—This paper compares the performance and tradeoffs of various backscatter imaging algorithms for the SeaWinds scatterometer when multiple passes over a target are available. Reconstruction methods are compared with conventional gridding algorithms. In particular, the performance and tradeoffs in conventional "drop in the bucket" (DIB) gridding at the intrinsic sensor resolution are compared to high-spatial-resolution imaging algorithms such as fine-resolution DIB and the scatterometer image reconstruction (SIR) that generate enhanced-resolution backscatter images. Various options for each algorithm are explored, including considering both linear and dB computation. The effects of sampling density and reconstruction quality versus time are explored. Both simulated and actual data results are considered. The results demonstrate the effectiveness of high-resolution reconstruction using SIR as well as its limitations and the limitations of DIB and fine-resolution DIB.**

***Index Terms*—Backscatter, QuikSCAT, rapidscat, reconstruction, sampling, scatterometer, SeaWinds, variable aperture.**

I. Introduction

MICROWAVE wind scatterometers such as the SeaWinds sensor [1] measure the normalized radar cross section (σ^o) of the Earth's surface from which the near-surface wind over the ocean can be estimated [2]. Though optimized for ocean wind estimation, the σ^o observations have proven useful in a variety of studies of land, vegetation, and ice, e.g., [2]–[8]. Essential to most of these applications is a method of generating maps or images of the surface σ^o on a uniform grid.

Algorithms for creating mapped images from noisy σ^o measurements are characterized by a tradeoff between noise and spatial and temporal resolution [9]–[11]. Conventional gridding techniques such as "drop-in-the-bucket" (DIB) gridding provide low-noise, low-resolution products, but higher spatial resolution products are possible using image reconstruction techniques [9], [11]. Both types of products have their strengths and weaknesses, and users must choose the processing approach that best suits their particular research application.

This work is motivated by the desire to improve the resolution of the real-aperture SeaWinds sensor using reconstruction techniques. The particular purpose of this paper is to compare and contrast conventional low-resolution techniques with high-resolution techniques for generating multiple-pass backscatter images from SeaWinds data using both simulation and actual data. The high-resolution image formation algorithms have been used for other active [9], [12] and passive sensors [11], [13]. This paper focuses on some of the issues associated with generating σ^o images of the Earth's surface using data from the SeaWinds sensor on the Quick Scatterometer (QuikSCAT) mission; however, the results apply to other SeaWinds-class sensors. The methods can also be applied to other scatterometers.

The paper is organized as follows: After some brief background, a review of scatterometer backscatter image reconstruction is provided that includes a derivation of the measurement spatial response function (SRF) for SeaWinds, as well as a discussion of several image formation algorithms. A discussion of the temporal and spatial sampling provided by QuikSCAT is given. Simulation is employed to compare and contrast the performance of the algorithms. Finally, actual data results are provided for both static and dynamic targets followed by a summary conclusion.

II. Background

The SeaWinds scatterometer has flown on multiple missions. The first two were the QuikSCAT in 1999 to the present and the Advanced Earth Observing Satellite–II (ADEOS-II) in 2003. For historical reasons, the SeaWinds sensor on QuikSCAT is referred to as QuikSCAT, while the SeaWinds sensor on ADEOS-II is known as SeaWinds [14]. RapidScat is the third SeaWinds mission. RapidScat is the slightly modified SeaWinds engineering prototype hardware flown on the International Space Station from 2014 to the present [15]. In addition, the Indian Space Research Organization (ISRO) Oceansat-2 scatterometer (OSCAT), which operated from 2009 to 2014, is very similar to SeaWinds [16], but with slightly different incidence angles (see [17] for a detailed comparison of OSCAT and QuikSCAT). These instruments comprise the to-date QuikSCAT era of Ku-band pencil-beam scatterometry. Additional Ku-band scatterometers are planned by ISRO: ScatSat launched in August 2016 and OceanSat-3 to be launched in 2018. The Chinese State Ocean Administration has launched or is planning to launch a number of rotating fan-beam Ku-band scatterometers, HY2A, HY2B, and HY2C.

The SeaWinds/QuikSCAT swath and scanning concept is illustrated in Fig. 1. OSCAT is similar [17]. The SeaWinds antenna spin rate is 18 r/min, producing an along-track spacing of approximately 25 km. As the antenna rotates, each beam traces a helix on the surface. SeaWinds alternately transmits 1.5

Manuscript received May 27, 2016; revised August 29, 2016 and October 8, 2016; accepted November 7, 2016. Date of publication November 30, 2016; date of current version May 24, 2017. *(Corresponding author: David G. Long.)*

The author is with the Department of Electrical and Computer Engineering, Brigham Young University, Provo, UT 84602 USA (e-mail: long@ee.byu.edu).

Color versions of one or more of the figures in this paper are available online at http://ieeexplore.ieee.org.

Digital Object Identifier 10.1109/JSTARS.2016.2626966

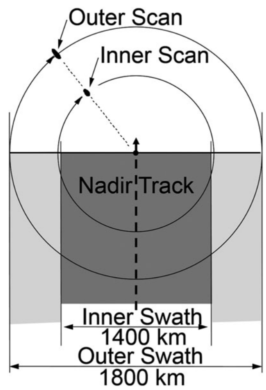

Fig. 1. Illustration of the QuikSCAT and SeaWinds observation geometry. Antenna feeds for inner horizontal (HH) polarization (H-pol) and outer vertical (VV) polarization (V-pol) beams share the same dish reflector, producing separate beams. The off-nadir pointing antenna rotates at 18 r/min, resulting in a circular scan at fixed incidence angles. Coupled with the along-orbit motion of the spacecraft, the resulting measurements are collected along a dual-helix pattern. A given point within the swath is first observed by at least one forward-looking beam, and later by at least one aft-looking beam. Within the inner swath, the point is observed by both antennas, while in the outer swath, the point is observed by only the outer scan.

TABLE I
NOMINAL SEAWINDS [1] AND OSCAT [18] MEASUREMENT CHARACTERISTICS

Sensor	Scan Beam	Polarization	Incidence Angle (deg)	Beam Footprint (km)	Slant Range (km)
SeaWinds	Inner	HH	46	35 × 44	1200
	Outer	VV	54.4	37 × 52	1600
OSCAT	Inner	HH	49	26 × 36	1400
	Outer	VV	57	30 × 68	1836

ms pulses and receives from each beam at 92 Hz pulse repetition frequency (PRF) [1], [14]. Table I summarizes the nominal measurement geometry for SeaWinds and OSCAT.

All of the SeaWinds-class scatterometers (SeaWinds, QuikSCAT, RapidScat, and OSCAT) provide measurements in two forms, termed "eggs" and "slices" [14]. Egg measurements correspond (essentially) to the full footprint of the antenna pattern on the surface, while multiple (4–10) slices are simultaneously estimated by transmitting a slow linear-frequency modulated (LFM) pulse (i.e., a chirp) and using on-board range/Doppler processing to resolve the footprint into smaller areas [1]. Fig. 2 illustrates how the measurement footprints for eggs and slices vary as the antenna rotates. Averaging over a larger area than a single slice, eggs have less noise and coarser resolution than the narrower slices.

Backscatter data from the QuikSCAT-era sensors have been used for wind and weather forecasting applications over the ocean. Backscatter data over land and ice have also been used in a wide variety of applications. Most of these applications employ gridded images or maps of the observed σ^o that combine multiple passes over a given target area. To support and facilitate these applications, the Brigham Young University Scatterometer Climate Pathfinder (SCP) project (www.scp.byu.edu) has generated an extensive and compatible set of conventional and enhanced-resolution scatterometer backscatter image datasets

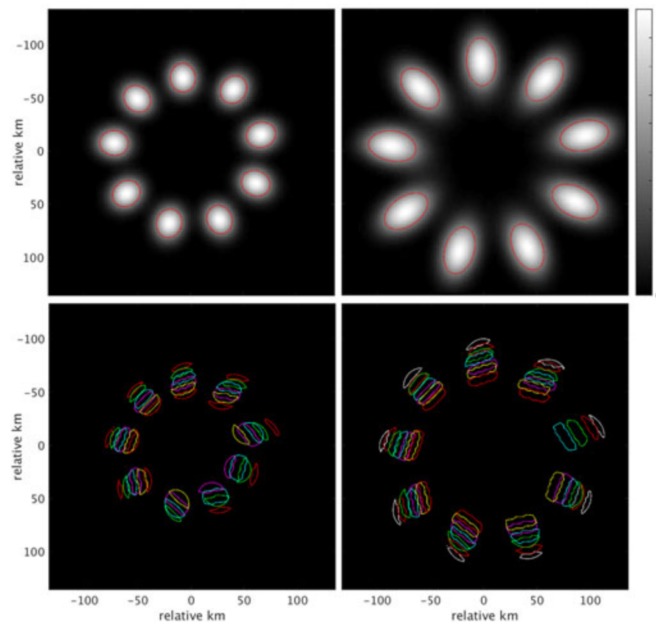

Fig. 2. Illustration of how the (top row) egg and (bottom row) slice SRFs vary as a function of antenna rotation angle for (left column) H-pol [the inner-beam] and (right column) V-pol [the outer-beam]. Contours are shown at − 3 dB from the peak response. For clarity, only contours are shown for slices. The linear-space egg SRF linear gain scale extends from zero to one. Selected SRFs from one rotation of the antenna are plotted. For the purposes of visualization, the selected SRFs have been horizontally shifted to appear close to each other since the actual radius is very large. Note the change in orientation of the footprints as a function of antenna rotation angle. The jagged edges of the slice contours are the result of the quantized grid on which the SRF is evaluated.

for all of these sensors, as well as for other scatterometers. The conventional-resolution images are based on classic DIB methods described in more detail below. Enhanced-resolution products with higher spatial resolution are produced using the scatterometer image reconstruction (SIR) algorithm [9], [19]. SIR uses signal reconstruction techniques to estimate σ^o on a finer grid than with simple DIB techniques. The higher resolution is possible using the SRF of the measurements.

III. SCATTEROMETER SRF

The effective spatial resolution of a gridded image is determined by the SRFs of the individual measurements from which the image is made, the grid resolution, and the image formation algorithm used. For the SeaWinds-class sensors, the SRF is determined by a combination of the antenna gain pattern, the observation geometry, and the on-board signal processing [2], [20]. This section describes the SRF for SeaWinds-class sensors.

The scatterometer-observed backscatter is related to the antenna pattern via the integral form of the radar equation. The measured radar echo power P_r for a particular measurement is given by [2]

$$P_r = \frac{P_T \lambda}{(4\pi)^3} \iint \frac{G_a^2(x,y) G_p(x,y) \sigma^o(x,y,\theta,\phi,t,p)}{R^4(x,y)} dxdy + \text{noise} \tag{1}$$

where P_T is the transmit power, λ is the radar wavelength, $G_a(x, y)$ is the effective two-way antenna gain at the surface, $G_p(x, y)$ is the processor gain at (x, y), and $R(x, y)$ is the slant range from the radar to the surface. The surface $\sigma^o(x, y, \theta, \phi, t, p)$ is a function of location (x, y), incidence angle θ, azimuth angle ϕ, time t, and polarization p (VV or HH). Both θ and ϕ are functions of x and y, but vary only slightly for a single measurement. The integration is over the region of nonnegligible $G_a G_p$. Technically, the sensor measures the temporally integrated power, i.e., the backscattered energy. For SeaWinds, the transmit pulse length is 1.5 ms; for RapidScat it is 1 ms. Even with a ground track velocity of approximately 7.5 km/s, the spacecraft moves only a few meters during the transmit pulse, while the resolution is in kilometers. Hence, the classic "stop and hop" approximation is appropriate and the integrand is essentially constant during the integration period for a single pulse.

A separate measurement of the noise-only power is made and subtracted from the measured receive signal power to estimate the signal-only power [1]. The reported backscatter measurement z is then given by [14]

$$z = \frac{P_r}{X} + \text{residual noise} \tag{2}$$

where the residual noise is the residual scaled variability after the noise estimation and subtraction step [1] and where the so-called "X-factor" X [20] is given by

$$X = \frac{P_T \lambda}{(4\pi)^3} \iint \frac{G_a^2(x, y) G_p(x, y)}{R^4(x, y)} dx dy. \tag{3}$$

It is apparent that the measurement z is the weighted spatial average of σ^o over the integration region. A given σ^o measurement z_i collected at the antenna rotation angle ϕ_i can thus be modeled as

$$z_i = \iint \text{SRF}_i(x, y) \sigma^o(x, y, \theta, \phi_i, t, p) dx dy + \text{residual noise} \tag{4}$$

where $\text{SRF}_i(x, y)$ is the SRF given by

$$\text{SRF}_i(x, y) = \frac{P_T \lambda}{(4\pi)^3} \frac{G_a^2(x, y) G_p(x, y)}{R^4(x, y)}. \tag{5}$$

Thus, the measurements z_i can be seen to be the integral of the product of the SRF and the surface backscatter. The nominal "resolution" of the backscatter measurements is typically considered to be the size of the 3 dB response pattern of the SRF and so conventional gridding is commonly done at this resolution. However, finer-resolution information is, in fact, contained in the measurements and is exploited using reconstruction processing [9], [19], [21]–[23].

Note that the measurements are an average of σ^o in spatial coordinates as well as in azimuth and incidence angles. The azimuth angle span for a given measurement is small and can be neglected. On the other hand, the variation in σ^o as a function of azimuth angle for different measurements is important and can provide useful geophysical information, e.g., wind direction over the ocean [24], snow dunes [3], [25], and sand dunes [29]. To deal with azimuth variation, either separate σ^o images have to be made for each azimuth angle [4] or images of the model parameters of an azimuth modulation model need to be generated. For example, [3], [25]–[27] use a Fourier series model for the azimuth variation observed in σ^o over snow fields on the great ice sheets. Due to the small variation in SeaWinds and OSCAT incidence angles, most imaging algorithms do not need to explicitly handle incidence angle variations, though a first-order correction can be used to normalize slice measurements to the egg incidence angle θ_{egg} when combining slice measurements, using the model equation

$$\sigma^\circ_{\text{slice}}(\theta) = \sigma^\circ_{\text{egg}} + B\,(\theta - \theta_{\text{egg}}) \tag{6}$$

where θ is the measurement incidence angle, σ^o values are expressed in dB, and B has the units of dB/deg. The value of B varies with surface characteristics, but has a global average of $\sim$0.15 dB/deg. The nominal incidence angles for QuikSCAT egg measurements are listed in Table I. The incidence angle at the center of the slices can span up to $\pm 0.5^\circ$ about the incidence angle at the center of the corresponding egg. Variations in incidence angle are somewhat larger ($\sim 1^\circ$) for RapidScat and OSCAT.

IV. Sampling

Geophysical processes vary in time and space. The scatterometer measurements are samples of these processes as expressed in σ^o. The scatterometer spatiotemporal sampling characteristics limit the time and space scales that can be accurately extracted from the σ^o measurements. It is thus helpful to review the details of the QuikSCAT temporal and spatial sampling. To do this, the sensor global coverage as a function of orbit is first considered. A more detailed view of the sampling is then presented.

A. Orbit Coverage

The wide swath of SeaWinds-class sensors, combined with the orbit, provide full coverage of every point on the globe, except a small region at the poles, at least once every two days [1]. Most areas of the planet are covered multiple times during this period. This coverage is illustrated with the aid of Fig. 3. In this figure, different panels show the coverage area of different numbers of orbit revolutions ("revs"), that are 101 min long. The retrograde, 98.6° inclination QuikSCAT orbit starts at the southernmost orbit node, moves northward, passes near the North Pole, and then moves southward, terminating at the southernmost orbit node.[1] As previously noted, a given point on the Earth is typically observed multiple times per day. The temporal spacing of the observations varies with latitude, but at a given point can be divided into two groups by the Local Solar Time (LST) (local time-of-day) of the observations [28]. Within each group, the observations are within a few hours of each other. The LSTs of the two groups differ by 12 h at the equator (6 A.M. and 6 P.M. LST for QuikSCAT and OSCAT,

[1]This QuikSCAT/SeaWinds orbit convention differs from the more standard convention used by OSCAT where an orbit starts at the ascending node equator crossing. The QuikSCAT/SeaWinds convention was chosen for convenience in processing winds over the ocean [14].

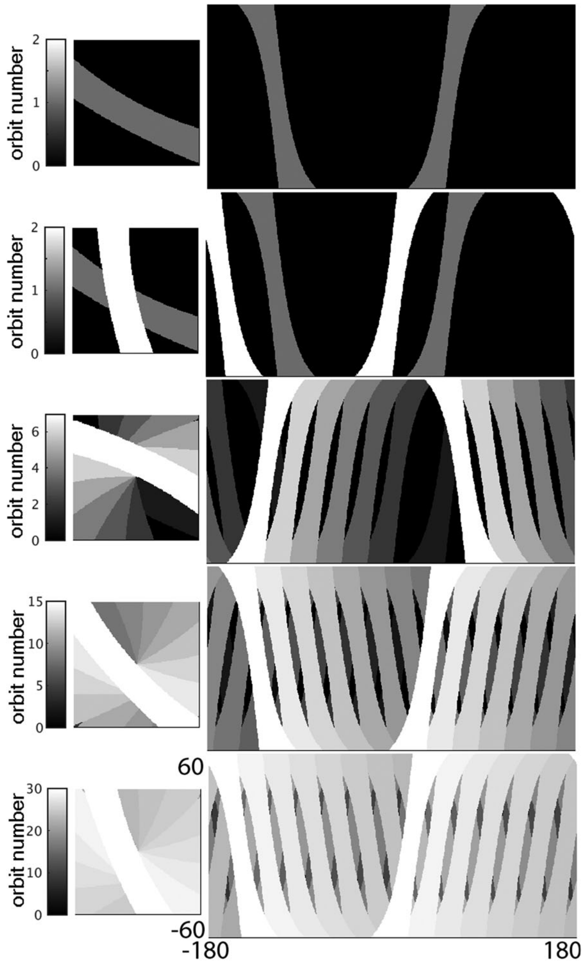

Fig. 3. Illustration of QuikSCAT coverage versus time. (Left column) Northern hemisphere polar view extending 4000 km from the pole at the image center. (Right column) global view. The latitude range shown extends $\pm 60^\circ$. (Rows from top to bottom) 1 rev, 2 revs, 7 revs, 15 revs ($\sim$1 day), 30 revs ($\sim$2 days). Each orbit number has a different grayscale value, with more recent orbits having a lighter color and covering previous orbits. Note that for visibility a different grayscale is used for each image.

and about 9:30 A.M. and 9:30 P.M. LST for SeaWinds). At high latitudes, there are more measurements at a given point, and the measurements occur at different LSTs.

B. Temporal and Spatial Sampling

For a given sensor pass over the target,[2] it is reasonable to treat σ^o as temporally constant. However, σ^o can vary from pass to pass due to changes in the surface backscatter characteristics resulting from changes in wind, freeze/thaw state, rain, vegetation moisture content, and motion of the target. When multiple passes are combined, such temporal changes can be expected to smear the resulting σ^o images, which ideally are the temporal average of the surface backscatter characteristics over the imaging period. When changes are slow, this is not an issue. For very rapid changes, single pass imaging can avoid smearing, but has limited spatial resolution.

[2]The maximum time difference between a fore-looking and aft-looking measurement in a single pass is $\sim$3.5 min.

A single pass over a target area provides an essentially instantaneous temporal snapshot of the backscatter at the time of the pass. Due to the spinning antenna, each point in the swath is observed at least twice on one pass: once by the antenna looking forward, and once by looking backward (see Fig. 1). The observations all occur within 3.5 min of each other. The next observation of a particular location must wait until a later orbit pass, which is at least 101 min later but can be longer. Thus, observation of rapidly evolving processes, such as wind, must be done on a single pass basis. However, dominant land and ice processes are more slowly evolving and multiple passes can be combined to reduce the noise at the expense of fine temporal resolution. Combining multiple passes provides denser spatial sampling, which can be exploited to estimate σ^o at higher spatial resolution and lower noise than is possible with a single pass. Thus, scatterometer sampling provides an opportunistic tradeoff between temporal and spatial resolution.

Freeze/thaw events and some vegetation processes exhibit a diurnal cycle. Since QuikSCAT and OSCAT sample at essentially only two different LSTs, details of the diurnal cycle cannot be fully resolved (RapidScat is in a nonsunsynchronous orbit, and thus can provide LST sampling [15]). Rain and melt/freeze events may be very rapid and can cause a step-change in σ^o. Precisely resolving such events can be difficult due to the limited temporal sampling. However, multipass images before and after the event are useful for detecting such events since the events induce long-term changes [6], [30]–[35]. Moving targets such as icebergs or sea ice may be blurred if their movement over the imaging period is greater than the equivalent of a few image pixels. Nevertheless, the multipass σ^o images are useful for locating and tracking such targets, which may not be possible with single-pass data [7].

The rotating antenna also provides sampling of the azimuth dependence of σ^o, sometimes termed "azimuth modulation," for each co-polarization. Over multiple passes, measurements are collected over a finite set of azimuth angles. As previously noted, during one pass, a given point is observed by forward and aft-facing antennas, providing two different azimuth angles. Ascending and descending orbit passes over the same point have different sets of azimuth angles. Each orbit in the orbital repeat cycle provides a slightly different set of azimuth angles, resulting in a wide diversity of azimuth observations. While most areas of the Earth exhibit limited azimuth modulation at the scale of the scatterometer observations, the azimuth diversity can be exploited to study areas with azimuthally dependent processes such as sastrugi (snow dunes) [3], [25], [27] and sand dunes [29].

The latitude and longitude locations of the individual egg and slice σ^o measurements are provided in the QuikSCAT Level-1B product files [14]. In order to create σ^o images, the measurement center locations are mapped to a grid (pixel) location using a map projection that converts latitude and longitude to the map coordinate system. The SRF for the measurement, which varies with the antenna rotation angle and orbit position, is similarly mapped through the map projection to compute the value of the measurement's SRF at each pixel of the image map.

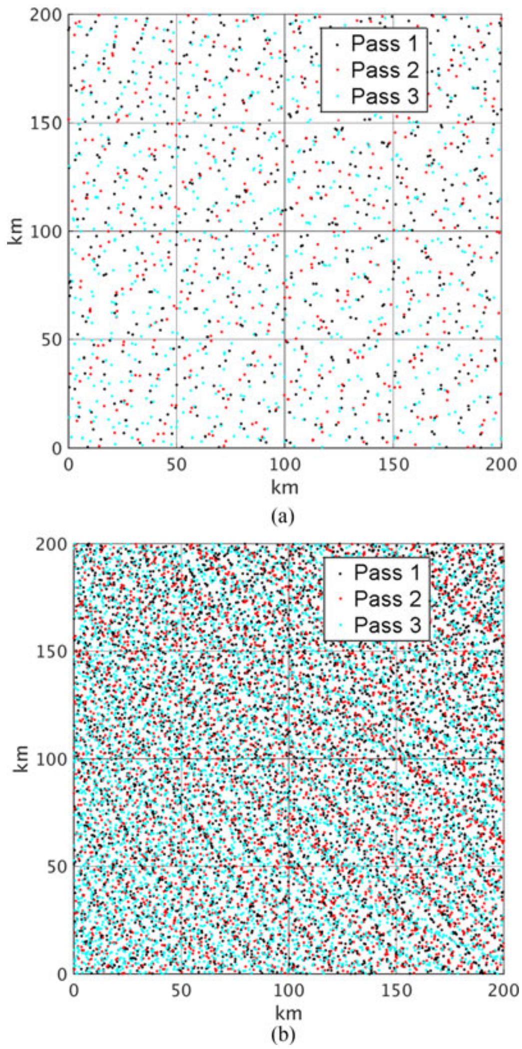

Fig. 4. Illustrations of the measurement locations within a small study area. (a) Eggs. (b) Slices.

To illustrate the spatial distribution of the reported measurement locations, the measurement center locations are plotted in Fig. 4 for single and multiple QuikSCAT passes over an arbitrary but representative area. The locations of both egg and slice centers are shown. The variation in sample locations with respect to the map grid is apparent. As suggested by the figure and compared to the footprint sizes (see Table I), the spatial sampling is quite dense, especially for slices. Note that while the sampling for a single pass is fairly regular, the effective sampling from multiple overlapping passes tends to be irregular.

C. Sampling and Reconstruction Theory

The goal in forming a σ^o image map is to estimate the backscatter properties of the surface from which the desired geophysical properties can be extracted. A σ^o map can be formed by merely gridding the data based on the location and averaging all measurements whose centers fall into the same map pixel grid. This method is known as "DIB" gridding and is a simple way to generate a σ^o image. The DIB grid size is typically approximately the footprint size. A more sophisticated approach is to use signal reconstruction techniques to produce higher spatial resolution. This approach uses both the measurement locations and the SRFs of the measurements.

Reconstruction processing techniques effectively assume the underlying signal (the backscatter) being sampled is band-limited, which is the only consistent assumption possible with sampled data [21]. Though not necessarily strictly true for an arbitrary σ^o field, the energy in the spectrum of most geophysical processes of interest tends to fall off at small scales. The spectrum of the SRF further restricts the energy in fine-scale portions of the spectrum of the σ^o field. Hence, assuming a band-limited σ^o field is not unreasonable.

For reconstruction, the backscatter at each point of a fine-scale pixel grid is estimated, producing a backscatter image or map. While the image is generated on a regular grid, the measurement locations are not aligned with the grid, and so the measurements form an irregular sampling pattern. Fortunately, there is a well-defined theory of signal reconstruction based on irregular sampling [36], [37] which can be applied to the problem [21].

The limit on the resolution of two-dimensional reconstruction from irregular samples is based on the Gröchenig δ-dense criterion [9], [36], [37]. The δ-dense parameter describes the largest rectangular box that contains a single sample center position. In effect, this is the worst-case spacing between samples. The δ-dense parameter is to irregular sampling what the Nyquist interval is to regular (uniform) sampling.

The Gröchenig criterion states that to recover a signal with wavenumber (spatial frequency) ω_0, the sampling must satisfy

$$\delta < \frac{\ln(2)}{2\omega_0} \tag{7}$$

where (for this application) δ is the largest dimension of the δ-dense rectangle. In contrast, the corresponding limit for regular (uniformly spaced) sampling with spacing δ_u is the conventional Nyquist criterion given by

$$\delta_u < \frac{1}{2\omega_0}. \tag{8}$$

Thus, for a given ω_0, irregular reconstruction requires a finer sampling density than regular sampling to ensure full signal reconstruction. Note that (7) implies that the finest resolvable spatial feature d for a given δ is

$$d > \frac{2}{\ln(2)}\delta \approx 2.89\delta. \tag{9}$$

For uniform sampling, this limit is

$$d > 2\delta_u \tag{10}$$

which confirms that regular sampling provides better resolution than an arbitrary irregular sampling for a given sampling density.

To derive the general reconstruction approach, the measurement equation (4) is discretized on the imaging grid to become

$$z_i = \sum_{j \in \text{image}} h_{\text{ij}} a_j \tag{11}$$

where a_j is the backscatter at the center of the jth pixel and $h_{\text{ij}} = \text{SRF}(x_l, y_k; \phi_i)$ is the discretely sampled SRF for the ith measurement evaluated at the jth pixel center, where h_{ij} is normalized so that $\sum_j h_{\mathrm{ij}} = 1$. In practice, the SRF is negligible some distance from the measurement center, so the sums need only be computed over a small area around the pixel. Equation (11) can be written as the matrix equation

$$\vec{Z} = \mathbf{H}\vec{a} \tag{12}$$

where $\mathbf{H}$ contains the sampled SRF for each measurement and $\vec{Z}$ and $\vec{a}$ are vectors composed of the measurements z_i and a_j, respectively. Even for small images, $\mathbf{H}$ is large and sparse, and may be overdetermined or underdetermined depending on the number and locations of the samples. Reconstruction of the surface σ^o is equivalent to inverting (12).

The iterative SIR algorithm [9], [19] is an example of a reconstruction algorithm specifically developed for scatterometer image formation. The SIR algorithm is a particular implementation of an iterative solution to (12). SIR approximates a maximum-entropy solution to an underdetermined equation and a least-squares solution to an overdetermined system. The first iteration of SIR is termed "AVE" (for weighted AVErage) and provides a simple reconstruction estimate. The AVE estimate of the jth pixel is given by

$$a_j = \frac{\sum_i h_{\mathrm{ij}} z_i}{\sum_i h_{\mathrm{ij}}} \tag{13}$$

where the sums are over all measurements that have nonnegligible SRF at the pixel.

The SIR iteration begins with an initial image a_j^0 whose pixels are set to be the AVE value defined in (13). Thereafter, the iterative equation for single-variate SIR is given by

$$a_j^{k+1} = \frac{\sum_i u_{\mathrm{ij}}^k h_{\mathrm{ij}}}{\sum_i h_{\mathrm{ij}}} \tag{14}$$

where

$$u_{\mathrm{ij}}^k = \begin{cases} \left[\frac{1}{2p_i^k}\left(1 - \frac{1}{d_i^k}\right) + \frac{1}{a_j^k d_i^k}\right]^{-1} & d_i^k \geq 1 \\ \frac{1}{2}p_i^k(1 - d_i^k) + a_j^k d_i^k & d_i^k < 1 \end{cases} \tag{15}$$

$$d_i^k = \left(\frac{z_i}{p_i^k}\right)^{\lambda} \tag{16}$$

where $d_i^k = (s_i/p_i^k)^{\lambda}$ with $\lambda = \frac{1}{2}$. The factor d_i^k is the square root of the ratio of a measurement to its forward projection at the kth iteration. The update term u_{ij}^k is a nonlinear function of both d_i^k and the previous image a_j^k. The sigmoid-like nonlinearity in (15) constrains the amount of change permitted during any one iteration, thereby minimizing the effects of noise [19]. Though not used in this paper, a spatial median filter can be applied to the image between iterations to further reduce the noise [19].

For scatterometers, SIR is implemented in dB [9], [19], i.e., the computation is done on $10\log_{10}(z_i)$ rather than on the linear-space value z_i as done in the radiometer version [11], [13] of the SIR algorithm. However, the linear-space form can be applied to scatterometer data. In considering the differences between linear and dB processing, recall the well-known fact that computing the arithmetic mean of values in dB is equivalent to computing $10\log_{10}$ of the geometric mean of the linear-space values [38]. With the measurements in dB, the reconstruction processing can be viewed as a form of weighted geometric mean filtering. Since it has been found that geometric mean filters are better at reducing Gaussian-type noise and preserving linear features than (linear) arithmetic mean filters [39], some performance advantage to dB processing is expected. Nevertheless, for completeness, this paper compares the results of the SIR algorithm using both linear-space and dB measurements. Similarly, the performance of the DIB gridding computation is compared when computed in both dB and linear-space backscatter measurements. The linear and dB computations yield similar, but slightly different results, due to the relatively high signal-to-noise ratio (SNR) of the measurements and limited signal dynamic range. As shown later, the resulting images are within an RMS of one-half a dB of each other.[3]

Reconstruction enables estimation of the surface σ^o on a finer grid than is possible with the conventional DIB approaches, i.e., the resulting reconstructed σ^o has a finer effective spatial resolution than DIB methods. The reconstructed signal is often referred to as having "enhanced resolution," though in fact the reconstruction algorithm merely exploits the available information to reconstruct the original signal at higher resolution than DIB gridding.

In practice, since the σ^o measurements are quite noisy, attempting full image reconstruction can produce excessive noise enhancement. To reduce noise enhancement and resulting artifacts, regularization can be employed, at the expense of resolution [21]. Regularization is a smoothing constraint introduced in an inverse problem to prevent extreme values or overfitting. Regularization results in partial or incomplete reconstruction of the signal [21]. It also creates a tradeoff between signal reconstruction accuracy and noise enhancement. SIR includes regularization achieved by prematurely terminating the iteration.

V. Gridding and Reconstruction

All algorithms that generate two-dimensional gridded images from sensor measurements are characterized by a tradeoff between noise, spatial resolution, and temporal resolution [10], [23]. Whatever image/gridding approach is used, the reported pixel values are some sort of average of the σ^o measurements over time, azimuth angle, incidence angle, and any backscatter change due to geophysical processes during the averaging interval. To handle long-term surface variations, separate short-term images can be formed and averaged, or a single long-term image can be created. The multiple short-term image approach is discussed further later. Alternately, a temporal model can be employed to explicitly account for the temporal variation. For example, a hydrological model might be useful for soil moisture imaging. In any case, to minimize noise, the desire is to average

[3]Measurement noise and surface variability give the σ^o measurements a probability distribution function (pdf) that is mapped and combined through the imaging algorithm to yield the pdf of the pixel estimates. Linear processing preserves the Gaussian pdf typically assumed for the σ^o measurement pdf, while dB processing treats the same input as log-normal. However, since many measurements are combined in the SIR processing, the law of large numbers predicts that the pdf of the pixel values is effectively Gaussian in either case.

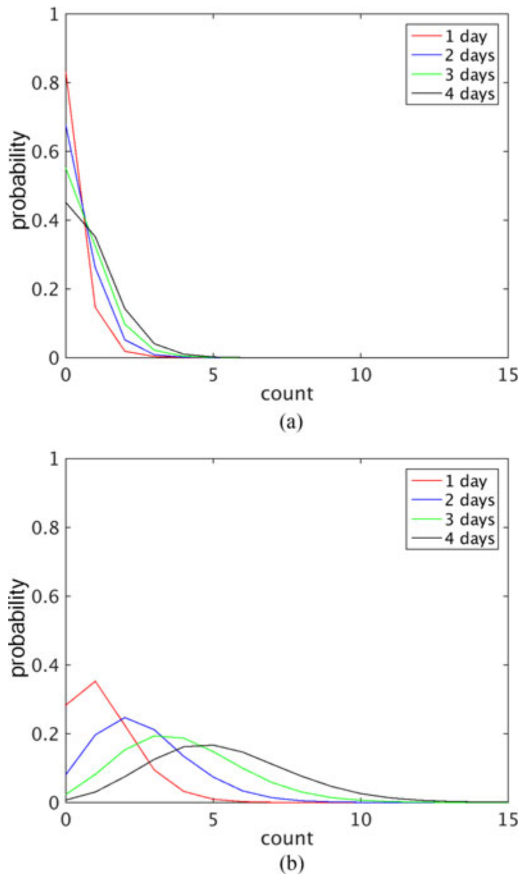

Fig. 5. Normalized histogram of the number of measurements that fall within one fine-resolution pixel for various time periods for the polar study region for (a) eggs and (b) slices.

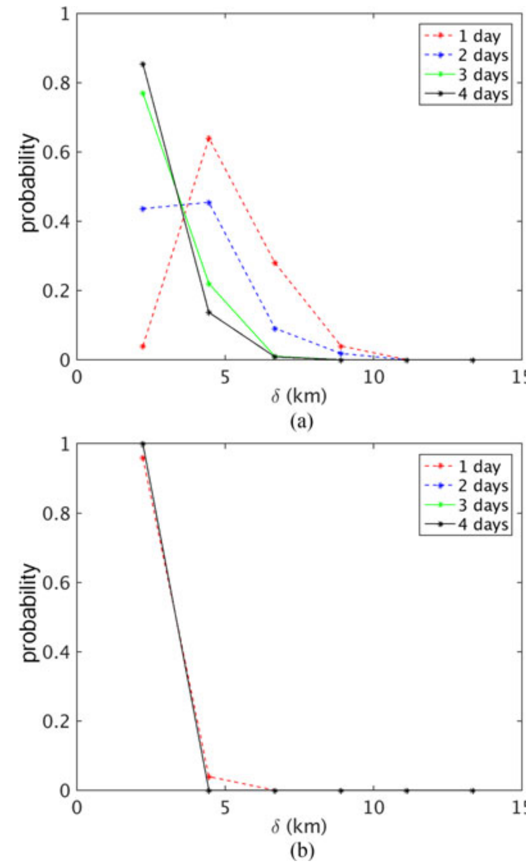

Fig. 6. Observed normalized histogram of the computed δ-dense metric for (a) eggs and (b) slices for various time periods for the polar study region.

as many measurements as possible in each pixel for the time period of interest.

The pixel size used in this paper is based on the compatibility with historical products. To be compatible with standard scatterometer products provided by the SCP project, the fine-resolution pixel size is set to 2.225 km. The low-resolution pixel size is set to ten times this value, or 22.25 km, which is approximately the nominal along-track sample spacing and simplifies embedding the fine-resolution grid within the low-resolution grid. Note that the *effective* spatial resolution of the imagery is coarser than the pixel size by at least a factor of two in order to meet the Nyquist criterion for the reported image.

To understand the tradeoff between time (orbits) and the number of available measurements that fall within a pixel, a representative study region spanning 10° of latitude is used to evaluate the distribution of the number of measurements that fall within each pixel. This is done based on actual reported QuikSCAT measurements over several periods in Fig. 5 for eggs and slices. For low-resolution pixels, all pixels have multiple egg and slice measurements. For fine-resolution pixels, not all pixels are hit, i.e., no measurement centers fall within them. With one day of data, only 20% of fine-resolution pixels contain at least one egg measurement center, though 70% contain slice centers. By four days, about 45% of pixels contain at least one egg center, while very few pixels do not contain a slice center. Thus, to ensure full coverage of an area using fine-resolution, multiple days are required, while coarse-resolution pixels need only one day.

A. Spatial Resolution

To help understand the tradeoff between imaging time and the δ-dense value, the δ spacing for each pixel for different time periods is computed. To do this, the measurement locations are quantized to fine-resolution grid centers, and the minimum spacing between each pixel center and the nearest measurement center is determined. This δ spacing varies and so the histogram of δ is computed for all pixels in the image. The normalized histogram is plotted in Fig. 6 for different time periods. Note that a δ density of better than 5 km is achieved within a single day for slices, but three days are required for eggs to achieve the same value. Based on the Gröchenig sampling criterion in (9), an image reconstruction resolution of 6.4 km can be supported for one day of slices and several days of eggs. For both conventional- (nonenhanced) resolution and enhanced-resolution images, the effective image resolution depends on the number of measurements and the precise details of their SRFs and spatial locations.

B. Temporal Resolution

Note that backscatter measurements combined into a single pixel may have different azimuth and incidence angles (though the incidence angle variation is small), and are collected at

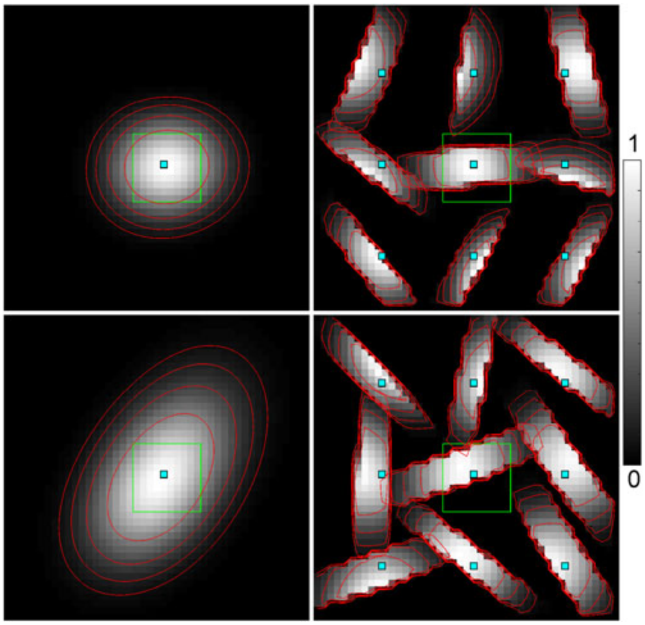

Fig. 7. Illustration of the measurement SRF for representative (left column) eggs and (right column) slices for both (top row) H-pol and (bottom row) V-pol. Contours are shown at -3, -6, -9, and -12 dB from the peak response. The image area is 100 km $\times$ 100 km. The large 22.25 km square box corresponds to the low-resolution DIB pixel size, while the small 2.225 km filled square box corresponds to the size of a single fine-resolution pixel. For clarity, slices are offset from the center as indicated by the positions of the small squares. The orientation (rotation) and shape of the slices and eggs change from location to location and versus time. The linear gain grayscale extends from zero to one.

different times. The resulting images represent a temporal average of the measurements over the averaging period. *This is true no matter what image formation or gridding technique is used.* As a result, there is an implicit assumption that the surface characteristics remain constant over the imaging period and that there is little to no azimuth variation in the true surface. Separate images can, of course, be created for different azimuth angles (which is done for enhanced-resolution wind retrieval [41]–[43]) or models can be used for the azimuth variation [3], [27].

In creating images from multiple passes, long-term surface variations, e.g., due to seasonal change, can be handled by creating either separate, short-term images to temporally sample the change or a single long-term average image to "average out" seasonal variations. Short-term sampling and averaging can avoid temporal aliasing that introduces errors, and it can also permit study of seasonal change and/or improve the long-term average by compensating for the seasonal change. Sudden backscatter change events within the imaging period, i.e., rapid changes compared to the imaging interval, tend to be averaged in the image. The precise averaging effects depend on the imaging algorithm. For DIB algorithms, which use simple averaging, the resulting pixel values are weighted by the number of measurements before and after the event so the pixel values are temporally weighted averages. The temporal weighting is conceptually similar for reconstruction algorithms, but is more complicated since their computation involves the spatial distribution of the measurements and includes measurements over a larger area.

Temporal inconsistency of the measurements can lead to image artifacts, regardless of the imaging algorithm employed, though the simple averages employed in conventional DIB can be expected to have smaller artifacts than reconstruction. This fact has led some [44] to incorrectly dismiss the utility of reconstruction. While it is true that large artifacts can be a concern when full reconstruction is attempted [21], in practice only partial reconstruction is done. The partial reconstruction limits both errors and artifacts, though it also limits the resolution improvement compared to full reconstruction. Artifacts resulting from temporal inconsistency can be useful for detecting short-term changes in images. In long-term images, the large number of measurements reduces potential artifacts, as seen in the actual data shown later. It should be noted that image artifacts associated with temporal change also occur in DIB images as well, particularly when DIB is attempted at fine resolution.

C. *DIB Algorithms*

A key advantage of DIB gridding is that the only information required is the measurement backscatter values and their locations. The general procedure is to define a rectilinear map pixel grid and map the measurement centers into the pixel grid. Then, all measurements falling within a particular pixel are averaged to produce the image pixel value. For DIB and a temporal stable target, the root mean square (RMS) pixel noise level is reduced by the square root of the number of measurements averaged in the pixel [12].

While the DIB pixel size can be arbitrarily set, the effective resolution of a DIB is, to zeroth-order, the sum of the pixel size plus the footprint dimension [11], so conventionally the pixel size is set to the size of the footprint. More precisely, the effective resolution of the DIB pixel is the size of the 3 dB contour of the pixel SRF. The pixel SRF is the average of the SRFs of the individual measurements, including their displacement from the pixel center. Since the measurement SRFs and locations within the pixel vary, the pixel SRF varies over the image. If the measurement SRFs are long in one dimension and have a variety of orientations within a pixel, the effective resolution of the average can be smaller than the pixel dimension [45].

There are several variations of the DIB method, including some that use overlapping pixels. In this paper, two are considered: the conventional coarse-resolution form already described, and oversampled DIB, termed "fine-resolution DIB," or fDIB. fDIB differs from DIB only in that finer pixels are used (fDIB is called the dense sampling method in [44]). As described below, fDIB can provide finer resolution than DIB but has the disadvantage that for a fixed time period, fewer measurements can be averaged into each pixel since the fDIB pixels are smaller than the DIB pixels, and some fDIB pixels may not have any measurements. To achieve the same number of measurements averaged into each pixel, a much longer integration period is required. Thus, fDIB is unsuited for short time intervals. Neither DIB nor fDIB requires information about the SRF.

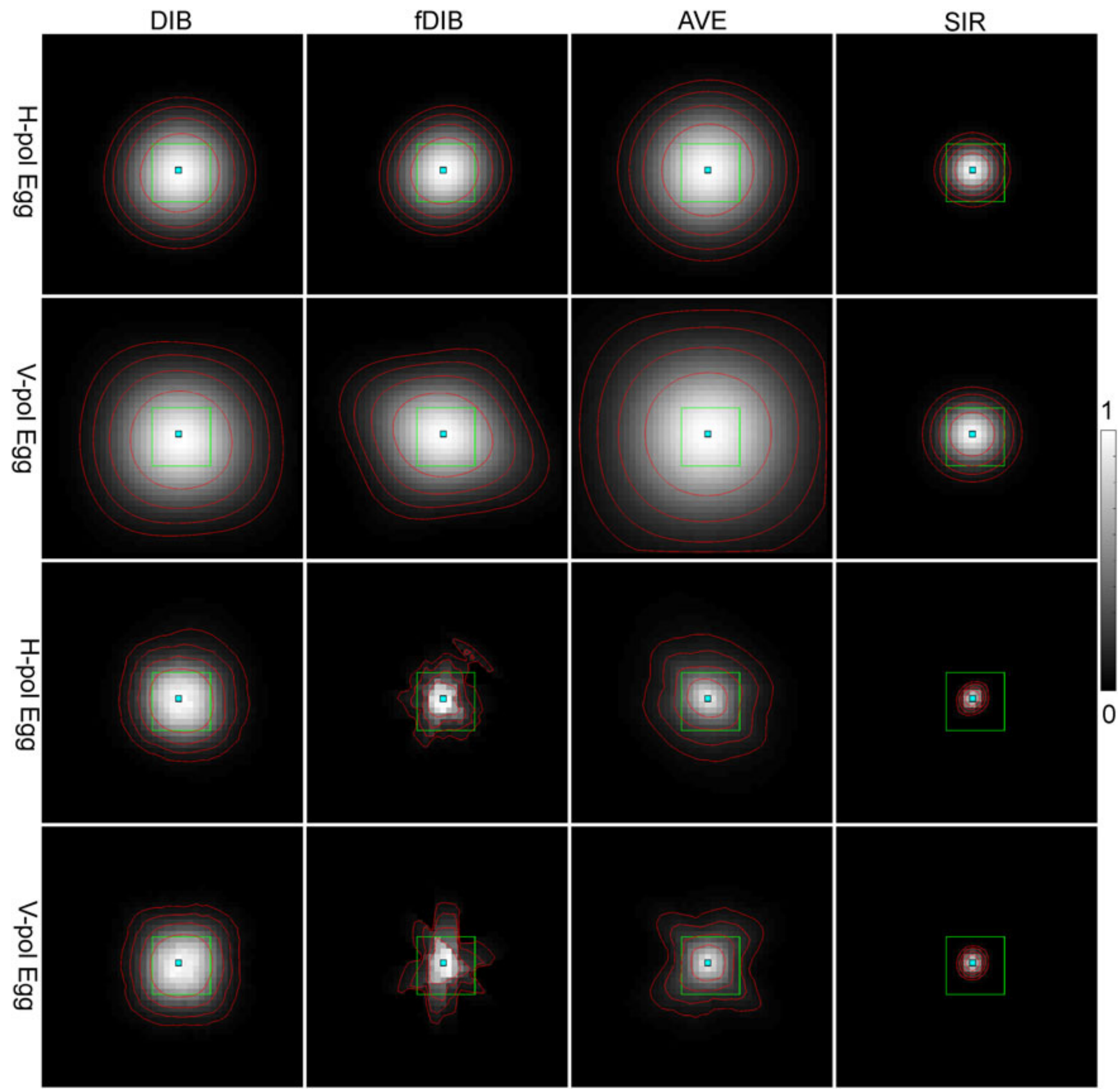

Fig. 8. Comparison of the effective SRF of pixels from different processing algorithms computed at the fine (2.225 km) pixel scale. (columns, left to right) DIB, fDIB, AVE, and SIR. (rows, top to bottom) H-pol eggs, V-pol eggs, H-pol slices, and V-pol slices. The size of each panel is 100 km × 100 km. Contours are shown at −3, −6, −9, and −12 dB from the peak response which is normalized to one. The linear grayscale extends from zero to one. The large 22.25 km square box corresponds to the low-resolution DIB pixel size, while the small 2.225 km filled square box corresponds to a single fine-resolution pixel. For the arbitrarily selected pixel location, the number of measurements included in each SRF is summarized in Table II.

D. SRFs and Reconstruction

In reconstruction algorithms, the effective SRF for each measurement is used to estimate the surface backscatter on a fine-scale grid. As previously noted, the SRF describes how much the backscatter from a particular location contributes to the observed backscatter measurements. It is specified by the antenna pattern and range/Doppler processing. The variation of the QuikSCAT SRFs versus antenna azimuth angle is illustrated in Fig. 2. The SRFs for a single egg for each beam are illustrated in Fig. 7. Also shown are example slices from various different eggs to illustrate the extreme variety of the slice SRFs. Note that the sharp edges of the slice SRFs are due to the rapid rolloff of the range/Doppler filter, while the smooth edges result from the antenna pattern rolloff. The relative sizes of the eggs and slices compared to the coarse- and fine-resolution grids can also be seen in the figure.

Explicitly computing the SRF for each measurement is computationally taxing and until recently has been impractical. Previously, the QuikSCAT SRF has been precomputed and parameterized to enable practical implementation of SIR [20]. To save memory and computation, the slice SRF was quantized to a value of 0 or 1, where a value of 1 was used within the 6 dB SRF contour and 0 was used elsewhere. This binary quantization is known as "quantized slice," and when used in SIR and AVE in this paper, as qSIR and qAVE, respectively. The performance of qSIR relative to full-SRF SIR is compared later.

When creating σ^o images, multiple backscatter measurements are combined. Knowing the individual measurement SRFs and their locations, the effective SRF of a particular pixel can be computed as illustrated in Fig. 8. The pixel SRFs for each case are based on the same measurements, though fDIB uses only some of the available measurements. Note that as expected for

TABLE II
NUMBER OF MEASUREMENTS INCLUDED IN THE SRF OF ONE PIXEL

Type	Polar-ization	DIB	fDIB	AVE	SIR*
		Algorithm			
egg	HH	176	2	1111	1111
egg	VV	108	3	1482	1482
slice	HH	1139	10	1139	1139
slice	VV	738	4	2133	2133

*First iteration of SIR. As SIR is iterated, the pixel SRF includes the effects of additional surrounding pixels.

DIB, the radius of the 3 dB contour corresponds to the nominal low-resolution pixel size. The larger V-pol egg SRFs produce larger pixel SRFs, but the slice SRFs are similar for both polarizations since the slice widths are approximately the same for both beams. The AVE egg SRFs are larger than DIB, and AVE slice SRFs are smaller. For eggs, the fDIB method provides a slightly smaller 3 dB contour than DIB. For slices, fDIB provides a significant reduction in SRF compared to DIB due to the varying orientations of the slices, albeit with much fewer measurements (see Table II). SIR provides the smallest, most-compact SRF. Compared to DIB, it can be concluded that

1) SIR provides finer SRF resolution in all cases,
2) AVE is better only for slices,
3) fDIB is not useful for eggs, and
4) while fDIB can provide better resolution than DIB, it comes at a cost of higher noise for the same integration period.

Note that since the SIR SRF is hard to directly compute, it is here computed as the impulse response for the pixel, whereas the other methods are computed directly by summing the measurement SRFs.

VI. IMAGE FORMATION PERFORMANCE SIMULATION

To compare the performance of the image techniques, it is helpful to use simulation where the true image is known. The results of these simulations inform the tradeoffs in applying the algorithms and understanding the limitations of each. The simulation uses the actual location, geometry, and SRF of real QuikSCAT measurements extracted and computed from QuikSCAT Level-1B files. From simulated noisy and noise-free measurements of a synthetic "truth" image, nonenhanced (DIB and fDIB), AVE, and SIR images are created, with error metrics mean and RMS determined for each case. This process is repeated separately for each polarization, though not all results are shown. Monte Carlo noise is added to the measurements using the system K_p for the actual measurements. An arbitrary "truth" image is generated with representative features including spots of varying sizes, edges, and areas of constant and gradient backscatter (see Fig. 9). The optimum values of the various algorithms' parameters can depend somewhat on the truth image used [9], [12]; however, other images considered in this study produce similar conclusions, so, for clarity, the results from only a single truth image are presented in this paper.

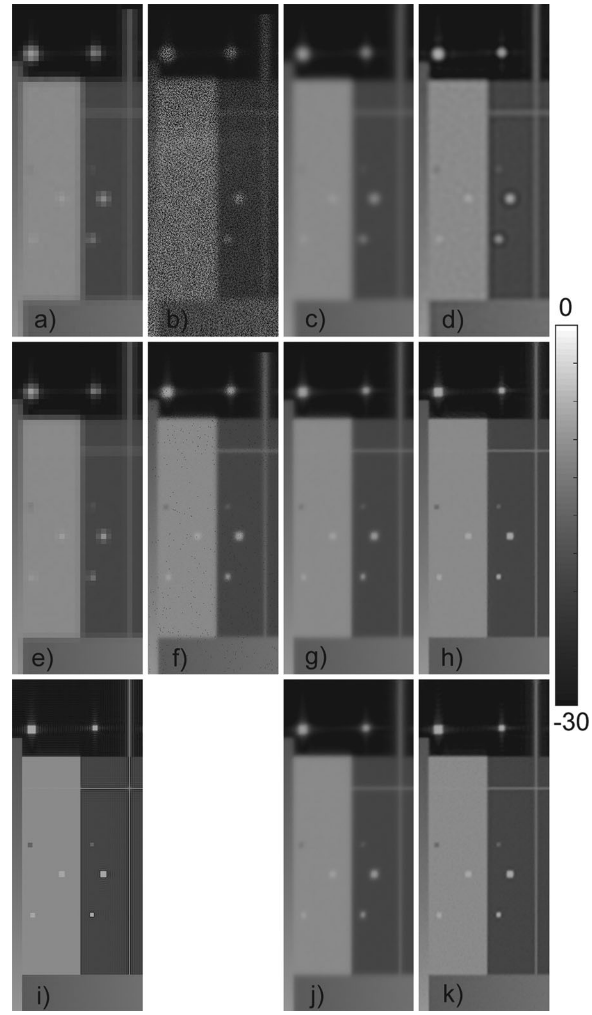

Fig. 9. QuikSCAT H-pol noisy simulation results for backscatter images. (a) DIB eggs. (b) fDIB eggs. (c) AVE eggs. (d) SIR eggs. (e) DIB slices. (f) fDIB slices. (g) qAVE slices. (h) qSIR slices. (i) Truth image. (j) AVE slices. (k) SIR slices. Error statistics are summarized in Table III.

In the simulation, the SRF and the measurement locations are computed from actual QuikSCAT data using a precision computation of the SRF based on each measurement's observation geometry, the measured antenna pattern, and the digital processor response. To apply the SRF in the processing, the SRF for each measurement is evaluated at the center of each pixel for which the SRF is greater than a minimum gain threshold of -30 dB relative to the peak gain.

Simulated DIB images are created by collecting and averaging all measurements whose centers fall within each low-resolution 22.25 km grid element. Simulated fDIB images are similarly computed but using the fine-resolution 2.225 km grid. When preparing images of different resolutions for display, the coarser resolution image is pixel replicated to match the pixels of the finer resolution image. The error is computed as the difference of each fine-resolution pixel.

In the simulation, the azimuth and incidence angle dependence of σ^o are ignored. Separate images are created for both noisy and noise-free measurements. Error statistics (mean, standard deviation, and RMS) are computed from the difference

TABLE III
ERROR STATISTICS IN dB FOR 4-DAY H-POL SIMULATION FOR VARIOUS IMAGE FORMATION METHODS

	Noise-free			Noisy		
Case	Mean	STD	RMS	Mean	STD	RMS
egg DIB	0.529	3.319	3.361	0.477	3.317	3.351
egg fDIB	0.481	3.273	3.308	0.446	3.325	3.354
egg DIB-L	0.609	3.409	3.463	0.607	3.407	3.460
egg fDIB-L	0.482	3.274	3.309	0.457	3.324	3.356
egg AVE	0.511	3.269	3.309	0.459	3.269	3.301
egg SIR	0.241	3.372	3.380	0.210	3.379	3.385
slice DIB	0.384	3.182	3.205	0.333	3.183	3.200
slice fDIB	0.381	3.269	3.291	0.338	3.286	3.303
slice DIB-L	0.539	3.354	3.397	0.539	3.354	3.397
slice fDIB-L	0.421	3.316	3.343	0.416	3.332	3.358
slice AVE	0.369	3.194	3.215	0.319	3.195	3.211
slice SIR	0.172	3.214	3.219	0.143	3.224	3.227
slice AVE-L	0.555	3.365	3.411	0.522	3.363	3.404
slice SIR-L	0.218	3.206	3.213	0.258	3.222	3.232
slice qAVE	0.373	3.210	3.232	0.322	3.211	3.228
slice qSIR	0.246	3.202	3.212	0.214	3.209	3.216
slice qAVE-L	0.522	3.362	3.402	0.555	3.367	3.412
slice qSIR-L	0.274	3.209	3.220	0.219	3.216	3.224

Image formation is with measurements in dB except for cases denoted by L that use non-dB (linear space) measurements. The value of linear-space error is converted to dB for display in the table.

between the truth and estimated images for each algorithm option. When used, the noise-only RMS is computed by taking the square root of the difference of the squared noisy and noise-free RMS values.

Fig. 9 illustrates a typical noisy simulation result. The error statistics are provided in Table III. In all cases, the mean error is small, so the RMS and standard deviation (STD) are similar. The nonenhanced results (DIB and fDIB) have the largest RMS errors, which is attributed to the errors along the region boundaries. The RMS error is the smallest for the SIR results. Visually, DIB and AVE are similar while the SIR images have better defined edges. The spots are much more visible in the SIR images than in the DIB images, though the SIR images have a higher apparent noise texture. The fDIB egg image has numerous “holes” with no data, while the fDIB slice image has only a few. Note that such holes are not included when computing the error statistics.

To help appreciate the differences between the algorithms, Fig. 10 shows the difference between the estimated and true images. For the most part, the errors are limited to ± 3 dB, though for the smallest spot in the lowest level area, the maximum error is 6 dB. The largest remaining errors are associated with edges. The spatial area effected by the edge error is the smallest for SIR and largest for DIB. Over smooth areas, AVE has the lowest variance and minimal texturing. Egg SIR has the greatest texturing and some overshoot along edges.

Creating the images in linear or dB space produces very similar, though not identical results. From Table III, the linear errors are slightly larger than the dB errors. The statistical differences between the images computed using linear and dB space measurements are summarized in Table IV. Unsurprisingly, the largest errors occur adjacent to large step-changes in backscatter in low backscatter regions of the image. Note that the

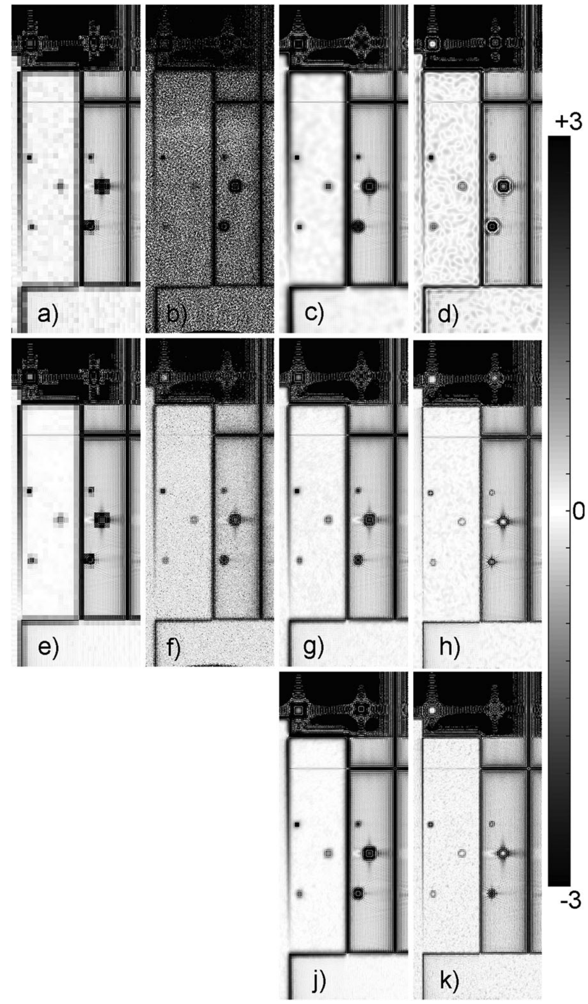

Fig. 10. Error difference (true-estimated in dB) between the estimated and true images shown in Fig. 9. (a) DIB eggs. (b) fDIB eggs. (c) AVE eggs. (d) SIR eggs. (e) DIB slices. (f) fDIB slices. (g) qAVE slices. (h) qSIR slices. (j) AVE slices. (k) SIR slices. Error statistics are summarized in Table III.

largest worst-case error (6.6 dB) occurs in the slice FDIB image, while the egg FDIB has the smallest worst-case (0.6 dB) error. The worst-case SIR algorithm differences are 5.4 and 4.5 dB for eggs and slices, respectively, which compare favorably to corresponding DIB differences of 1.9 and 4.0 dB. Because STD values are small ($<$0.5 dB), and significantly less than the signal reconstruction error ($\sim$3.3 dB), either processing approach can be used for most applications.

A. SIR Truncation

Theoretically, SIR should be iterated to convergence to ensure full signal reconstruction. This can require hundreds of iterations [9]. However, continued SIR iteration with noisy measurements also tends to amplify the noise in the measurements. The reconstruction error declines with continuing iteration while the noise increases. Truncating the iteration enables a tradeoff between signal reconstruction accuracy and noise enhancement. Truncated iteration results in the signal being incompletely reconstructed, but with less noise.

TABLE IV
STATISTICS OF THE DIFFERENCE (IN dB) BETWEEN LINEAR AND dB-COMPUTED IMAGES FOR VARIOUS CASES

Algorithm	Mean	STD	Worst-case
egg DIB	−0.135	0.227	1.9
egg FDIB	−0.011	0.028	0.6
egg AVE	−0.249	0.484	3.8
egg SIR	−0.090	0.484	5.4
slice DIB	−0.214	0.440	4.0
slice FDIB	−0.081	0.195	6.6
slice AVE	−0.239	0.469	4.6
slice SIR	−0.064	0.339	4.3
slice qAVE	−0.205	0.412	4.5
slice qSIR	−0.039	0.293	4.0

Subjectively, as the number of iterations of SIR is increased, image features and the contrast improves. Computing the RMS error for each iteration of SIR provides insight into the tradeoff between the number of iterations, signal error, and noise error. Fig. 11 plots the mean and RMS errors versus iteration. The noise power grows with increasing iterations while the signal error drops. The total RMS error at first declines with iteration, reaches a minimum, and then begins to climb again as the rate of signal improvement declines. There is thus an optimum number of iterations of SIR that minimizes the total RMS error. Iterating beyond this point continues to improve the signal error, but the noise error is also enhanced. Thus, the SIR iteration need not be continued to convergence, i.e., to full signal reconstruction, but can be prematurely terminated to optimize the overall error performance. The result is only "partial reconstruction" which, though having incomplete signal reconstruction, has the smallest total error. Recall that a nonlinearity is included in the SIR algorithm to help minimize the effects of noise and artifacts. The non-linearity has no effect at convergence [9].

Plotting the signal reconstruction error versus noise power increase as a function of iteration number in Fig. 12 can provide additional insight. These curves are dependent on the scatterometer SNR and to a lesser degree on the true image, but they are representative. In general, the optimum number of iterations corresponding to the minimum RMS error depends on the signal spectrum, the noise level and spectrum, the sampling density, and the pixel resolution. However, the smoothness of the tradeoff curves provides flexibility in selecting the number of iterations. In this paper, a value of 20 SIR iterations is selected. This values provides good signal performance and only slightly degraded noise performance. Since there can be some scene dependence, ideally one would optimize the number of iterations for each case. However, in practice, a single fixed value works well, and simplifies implementation. Furthermore, the fixed termination insures that images have similar noise characteristics. In Table III, it can be seen that the overall error performance of the truncated SIR reconstruction exceeds the alternatives.

In summary, SIR provides better spatial resolution and lower overall RMS error than conventionally gridded (DIB) products. The reconstruction increases noise, but this is offset by reduced RMS signal error due to the increased spatial resolution. The total error can be controlled by the number of iterations which provides an ad hoc way to trade off noise and resolution.

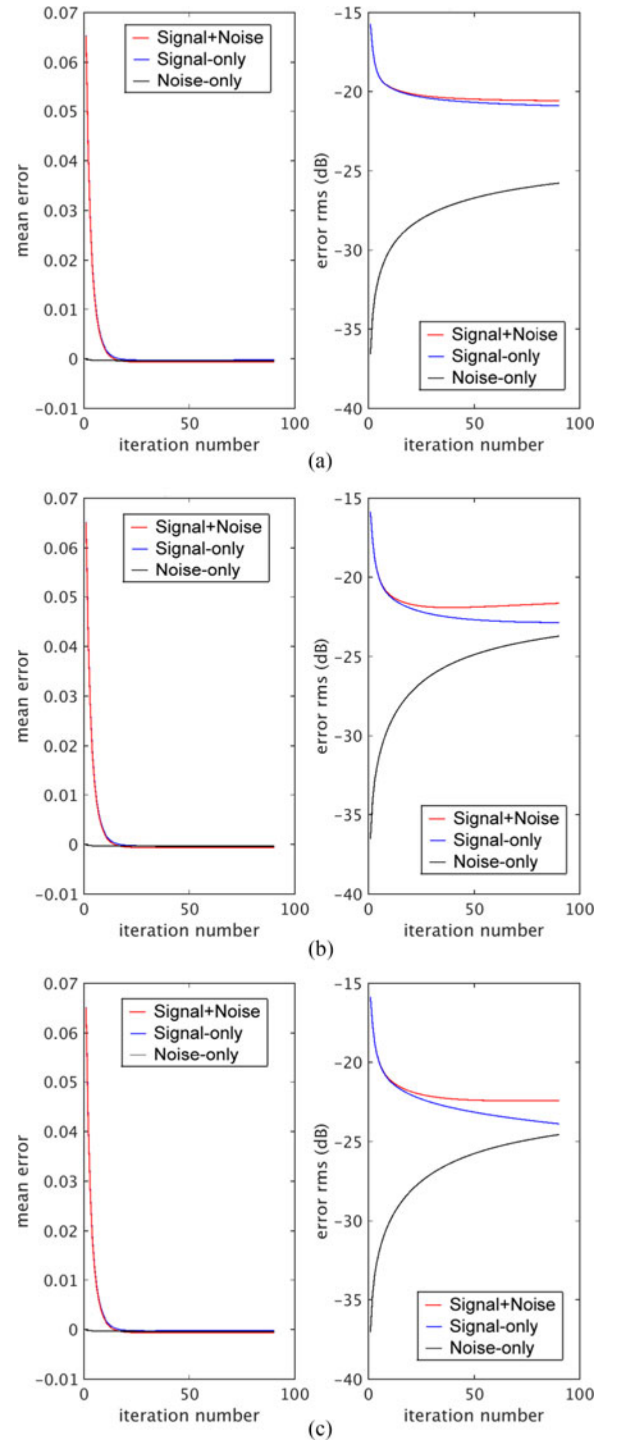

Fig. 11. SIR reconstruction error versus iteration number for (panel a) eggs, (panel b) quantized slices, (panel c) slices. In each panel, the left plot is the mean error expressed in linear space, while the right plot shows RMS error in dB. The noise-only RMS error is computed as the RMS difference between the noisy signal+noise image and the noise-free signal-only image. The minimum RMS error is at about 20 iterations for slices and somewhat higher for eggs.

The most significant conclusion is that due to the noise in the measurements, only partial reconstruction is desired to avoid excessively enhancing the noise. This has the fortunate by-product of also reducing computation requirements for SIR.

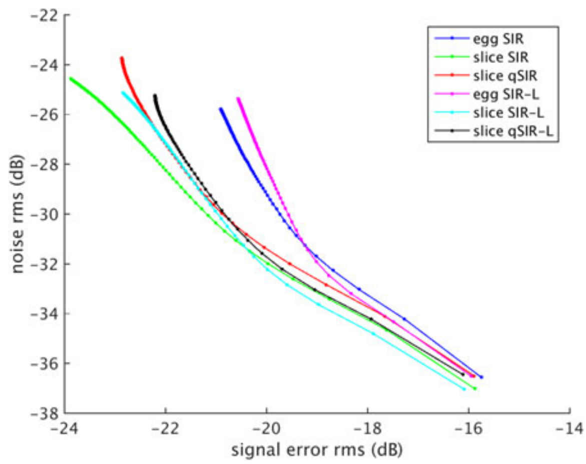

Fig. 12. SIR RMS noise error versus RMS signal error for various algorithm cases for the H-pol simulation. Note that the first iteration of SIR is at the far right. As SIR is iterated, the curve moves to the left, i.e., the number of iterations increases from right to left. In the legend, -L denotes use of linear measurements while the other cases use dB space measurements.

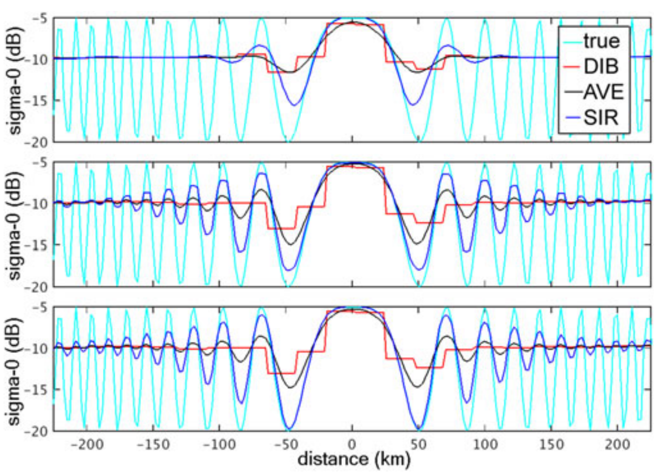

Fig. 13. SIR-spectral simulation results showing vertically averaged pixel rows. (top panel) Eggs. (center panel) Quantized slices. (lower panel) Slices. Color key for lines is: (cyan) true image, (red) DIB, (black) AVE, (blue) SIR.

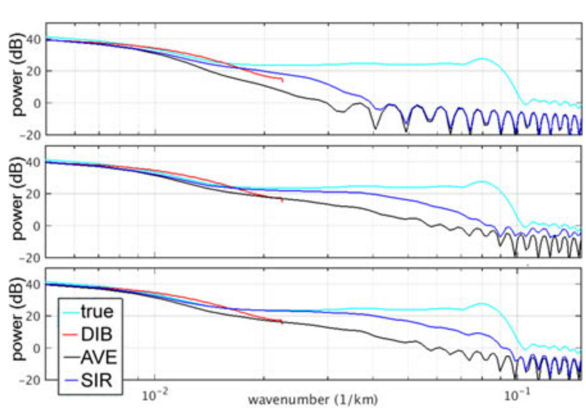

Fig. 14. Computed spectra of vertically averaged rows. (top panel) Eggs. (center panel) Quantized slices. (lower panel) Slices. Color key for lines is: (cyan) true image, (red) DIB, (black) AVE, (blue) SIR.

B. Spectral Analysis

The effective resolution of the reconstructed image can be difficult to quantify due to the variable SRF and spacing of the measurements. However, the effective resolution can be estimated with a simple analysis. Following [12], a synthetic true image is created with a horizontal LFM chirp in one row. The chirp extends from a constant to a band-limited 10 km sine wave. For simplicity, all image rows are identical. The image is reconstructed from simulated measurements of the true image. The reconstructed image is then row-averaged to summarize the results as a one-dimensional plot (see Fig. 13). In this plot, the chirp in true backscatter swings up and down from -20 to -5 dB as a function of distance. Most of the methods are able to reasonably represent the main center hump, but have varying degrees of accuracy in reproducing the higher frequency portion of the waveform. In particular, the DIB method can only coarsely represent the signal. AVE does better than DIB, while SIR does better than both. As expected, the egg measurements have the least high-frequency reconstruction capability, followed by the quantized slices. The full slice reconstruction for SIR is able to accurately represent the first few swings of the chirp, though its performance progressively degrades as the chirp frequency increases.

These observations are confirmed when examining the spectra of the one-dimensional signals, which are computed using Welch's method (see Fig. 14). Since each spectrum is symmetric, only one-half is shown. The spectra of the reconstructed egg images follows the behavior of the truth spectrum down to a wavenumber of about 0.02 km^{-1} (33 km) before falling off more quickly. As expected, the slice spectra extend further with less attenuation than the egg spectra, with the SIR spectra extending as far as the true signal spectra to 0.09 km^{-1} (11 km), though attenuated. The SIR spectra are less attenuated than the AVE spectra but both recover more frequency content than DIB. Coverage holes preclude comparing fDIB results for the four-day imaging period considered.

VII. Actual Data

While the previous results are based on simulation, this section uses actual data. The purpose of the analysis is to demonstrate and compare DIB and fDIB with enhanced-resolution imaging methods for different time periods for both constant and temporally varying surfaces.

To enable the detailed comparison of the algorithms for a four-day integration period with a constant surface, a small 580 km $\times$ 1400 km study area extending from the Antarctic coast into the interior is selected, see region (a) in Fig. 15. The study area includes a coastline, an area of ice-covered ocean, coastal mountains, and interior snow dunes. As the time period is mid-winter, no temporal change is expected, though some azimuth backscatter variation over the snow dunes may be present [3], [25]–[27]. In this paper, azimuth modulation is ignored in processing the data. The results of applying the various algorithms are shown in Fig. 16. While good quality DIB, AVE, and SIR images could be created with shorter time periods, a four-day

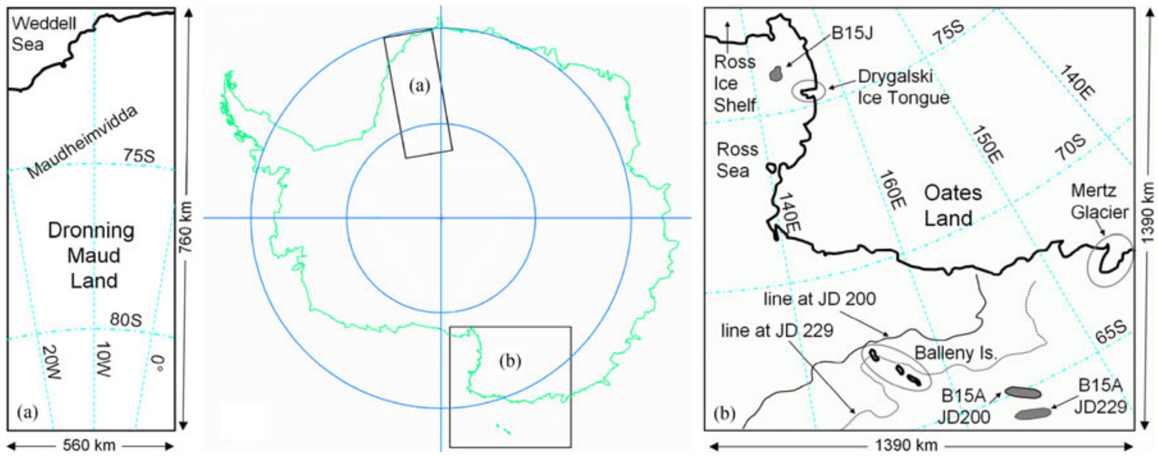

Fig. 15. Map of the locations of actual data study areas over Antarctica, and maps of the individual study areas with annotation of selected features. Note that the scales are different for each region.

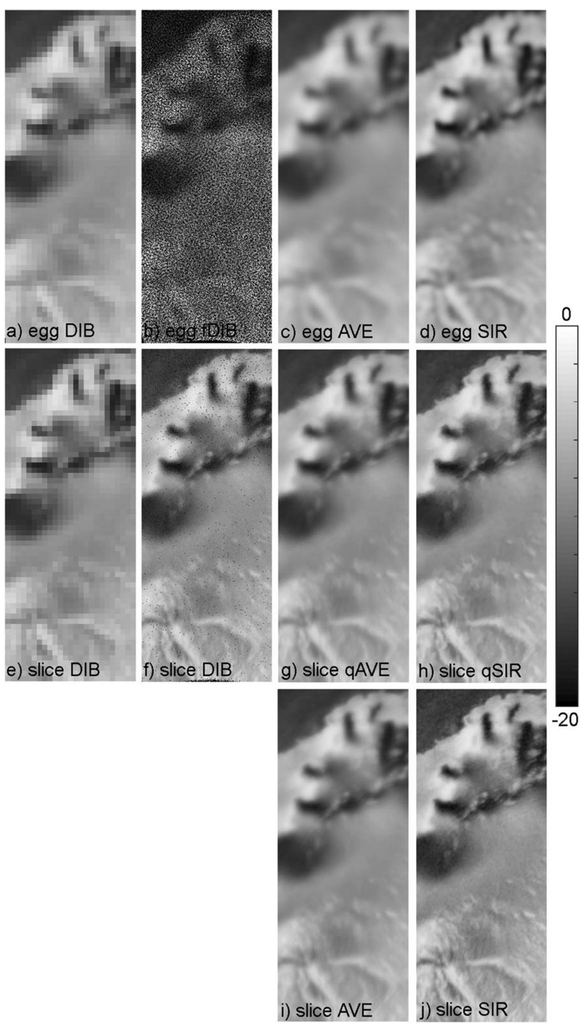

Fig. 16. Polar study area QuikSCAT H-pol σ^o images created from four days (254–257, 1999) of data for different cases: (top row) eggs, (center row) quantized slices, and (bottom row) slices. The columns are, from left to right, DIB, fDIB, AVE, SIR. The grayscale extends from -20 to 0 dB. The linear and dB processing are visually similar and so only the dB measurement images are shown.

period is selected so that the fDIB egg images contain enough valid pixels to create recognizable images. A longer period is needed to fully fill-in fDIB for either eggs or slices.

A visual comparison of the images in Fig. 16 reveals improved detail in the SIR images compared to the DIB images. Note that when using actual data, the true backscatter values are not known, so the reconstruction error cannot be computed. As expected, the DIB images are blocky, while the high-resolution images exhibit finer resolution. The slice fDIB image closely resembles the qSIR and slice SIR images, but still has missing pixels. Since the number of measurements averaged into each fDIB image pixel is much smaller than for the other cases, a higher level of noise is expected in the fDIB images compared to the other images. Subjectively, the SIR images have the highest contrast, minimal noise, and appear more detailed than the other images.

To study the effects of temporal variation on the image data, a large study west of the Ross Sea over Oates Land is defined [see region (b) in Fig. 15]. Constant over land, the study area includes moving and stationary icebergs and moving sea ice. A boundary line between older, bright sea ice, and darker, new ice moves in response to ocean currents and katabatic winds off the Ross Ice Shelf. The line extends diagonally south of the Balleny islands which show up as three bright shapes in the lower center of the image. Over the 30-day period, variable katabatic winds blowing off the Ross Ice Shelf push the sea ice north (down) and westward (right), creating bright new ice east (left) of iceberg B15J. Iceberg B15J remains stationary over the 30-day period considered, while iceberg B15A shifts downward and rotates. Other bright features in the image include the Drygalski ice tongue and the tongue of the Mertz glacier. These appear bright due to high σ^o resulting from volume scattering from buried ice features.

Fig. 17 compares qSIR images created from different periods of time. One-day images from the first and last day of a 30-day period in 2007 are compared to a four-day image from the start of the period and an image created from the full 30-day set of measurements. The two one-day images are less sharp and have more perceptual noise than the longer images.

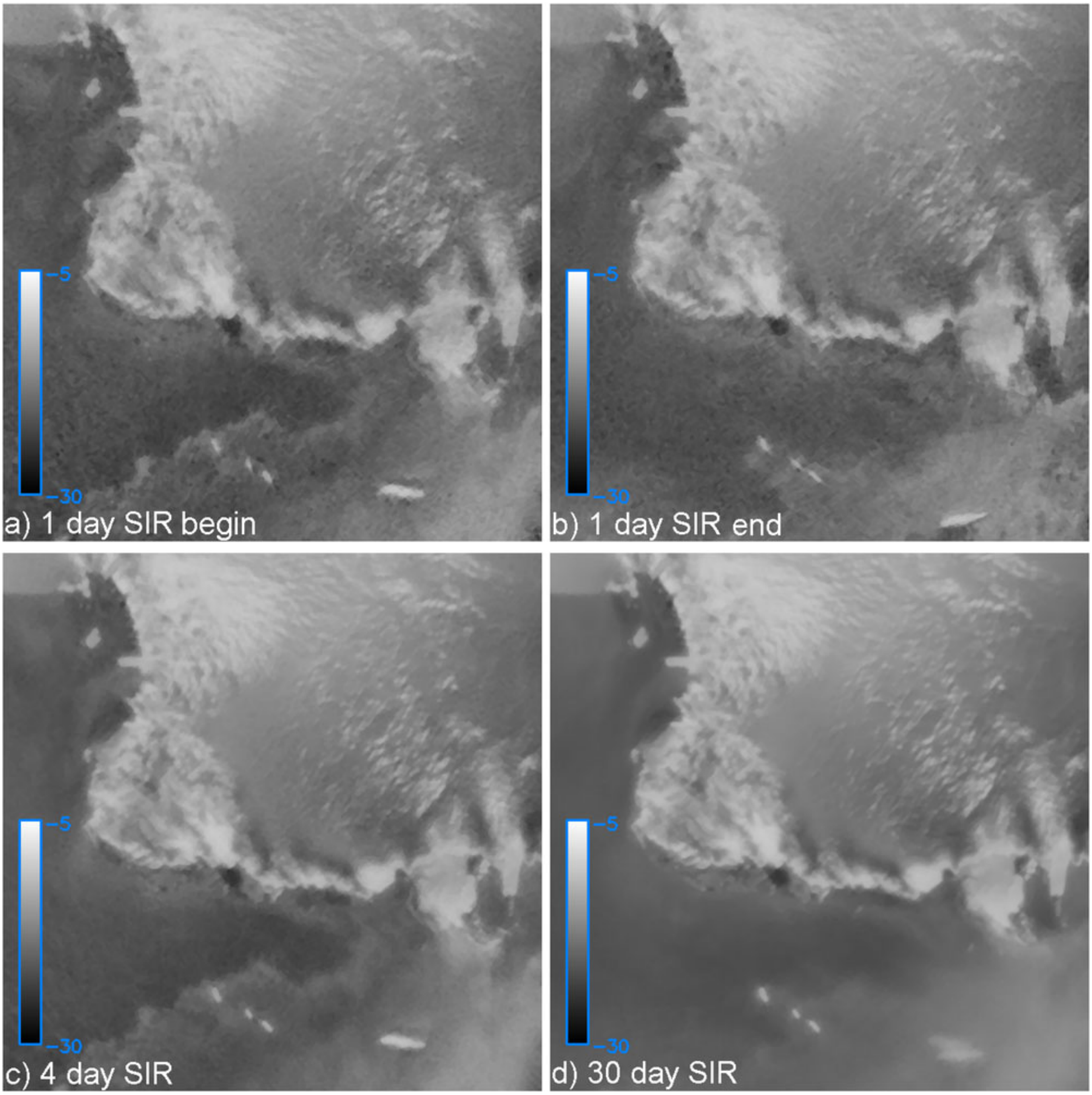

Fig. 17. QuikSCAT quantized SIR (qSIR) V-pol σ^o slice images spanning different time periods in 2007. (a) 1 day, JD 201. (b) 1 day, JD 229. (c) 4 days, JD 200–203. (d) 30 days, JD 200–229.

Clearly there are significant dynamic events occurring during this 30-day period as revealed by comparing the one day images from the start and end of the period. Note that sea ice in the 30-day image is smeared, and iceberg B15A appears in two places. From a time series of short-time images, not all of which are shown, this is a reasonable expectation for the average backscatter over this period. Observe that the subjective sharpness of the 30-day image is not much improved compared to the four-day image, suggesting that there is little resolution advantage to the longer period since at the grid resolution used, the spatial sampling density is not improved. Instead, the longer time period provides only more samples that improve the SNR, confirming the tradeoff between temporal resolution and noise reduction. Smearing effects can be minimized by using a time series of shorter images to study the evolution of the sea ice backscatter and the motion of the icebergs. The enhanced-resolution images can be compared with DIB and fDIB images in Fig. 18. In spite of temporal variation and measurement noise, the reconstructed images exhibit appropriate, desirable behavior without extreme values, and provide improved resolution and noise reduction.

Finally, a comparison of 4-day and 30-day slice DIB and fDIB images is shown in Fig. 18. It is apparent that the 30-day fDIB image is very similar to the 30-day qSIR image, though

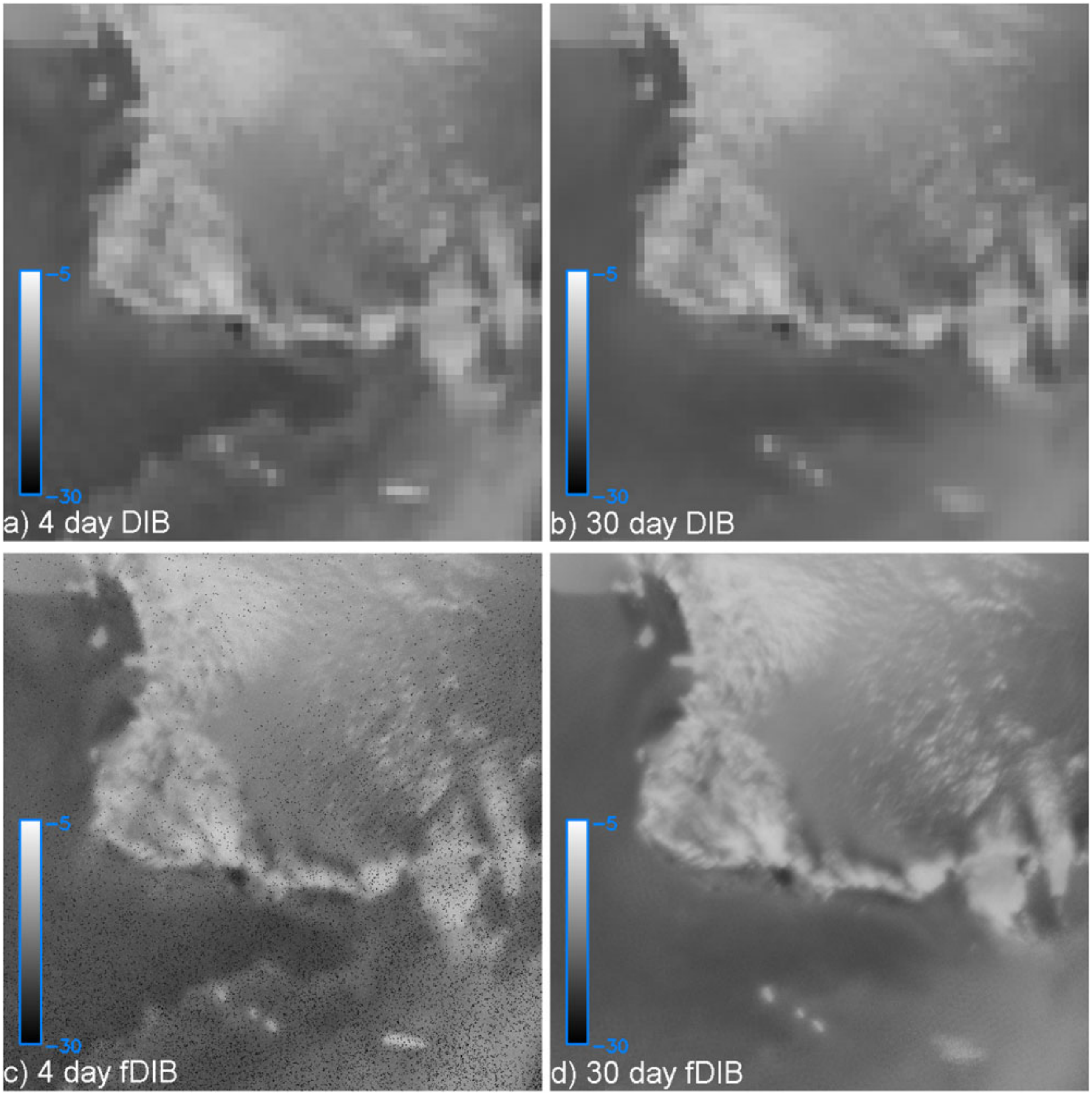

Fig. 18. QuikSCAT DIB V-pol σ^o slice images spanning different time periods in 2007. (a) DIB 4 day, JD 200–203. (b) DIB 30 day, JD 200–229. (c) fDIB 4 days, JD 200–203. (d) fDIB 30 days, JD 200–229.

with careful inspection it can be seen that the fDIB image is noisier and has texturing artifacts, particularly in the lower right. The texturing is due to high noise levels in pixels that contain few meaurements. A key observation from this image is the occurrence of temporal change artifacts in fDIB images, which leads to the conclusion that fDIB should not be used when temporal change is expected. The qSIR image, which exhibits consistent smoothing, is a better representation of the average conditions over the 30-day period. The four-day fDIB has many unfilled pixels, and has subjectively lower resolution than the four-day qSIR image. The fDIB and qSIR images resolve much finer features than the DIB images.

VIII. Conclusion

Single pass scatterometer backscatter data are commonly used for wind retrieval, but have coverage gaps over land and ice regions. Combining multiple passes fills coverage gaps and enables generation of backscatter images with reduced noise via measurement averaging. Exploiting the measurement SRF using reconstruction algorithms improves the resolution of the backscatter images. Since they are temporal averages of the radar backscatter over one or more days, multipass backscatter images provide better coverage and reduced noise. As discussed previously, they have wide application in studies of land, vegetation, and ice. Essential to most of these applications is a method of generating maps or images of the surface σ^o on a uniform grid on the Earth's surface.

A number of multipass backscatter image algorithms have been proposed over the years. Since no single algorithm can meet the needs of applications of the backscatter data, this paper has compared the performance of several common algorithms, including conventional DIB gridding, fDIB gridding, and the AVE and SIR enhanced-resolution imaging algorithms for creating multipass backscatter images from SeaWinds-class scatterometers. This paper has explored the limitations and strengths of the algorithms using the RMS and STD of the backscatter error as simple, general metrics.

All of the algorithms can average either linearly expressed or dB measurements. For land and ice imaging, where the SNR is relatively high, the results are very similar (within a STD of $<$0.5 dB). Furthermore, based on simulation, the STD of linear-dB differences are significantly less than the STD of the error ($\sim$3 dB) in the backscatter images. This suggests that for most applications, either computation method can be used in any of the algorithms.

Easy to compute and not requiring any information about the SRF, DIB provides only low-resolution images. Also not requiring the SRF, fDIB can produce high-resolution images, though it is noisier and more sensitive to the sampling distribution and to temporal change. fDIB requires a much longer integration period to ensure full coverage, and with fewer measurements averaged into each pixel, fDIB is noisier than DIB and the other algorithms. On the other hand, for long time periods with limited temporal variation, it can provide good spatial resolution without SRF information.

The iterative SIR algorithm provides the highest resolution by exploiting knowledge of the measurement SRF. SIR is equivalent to inverting the full matrix reconstruction matrix for the entire image but is regularized by truncating the iteration, resulting in only partial signal reconstruction. The truncation enables a tradeoff between noise and resolution. With an appropriate iteration count, SIR is shown to provide the minimum total RMS error when using noisy scatterometer measurements. The resulting images provide higher spatial resolution surface backscatter images with smaller total error compared to DIB and fDIB.

All of the algorithms (DIB, fDIB, AVE, and SIR) create backscatter images that are temporal averages over the imaging interval and thus have some of the same limitations when faced with temporal change during the imaging interval. To account for long-term changes, multiple short-term images that cover the long-term period can be used, though the minimum imaging period for fDIB makes this difficult when there is rapid change. Providing higher resolution than DIB, SIR images are quite robust to temporal change with slice SIR providing the best (better than 11 km) spatial resolution over two days for the scatterometers considered. For comparison, DIB provides an effective spatial resolution of $\sim$50 km for the same period, while fDIB does not provide adequate coverage to be useful. For QuikSCAT, increasing the imaging period beyond four days primarily reduces the noise, and has little impact on the spatial resolution, which is consistent with the δ-dense sampling of QuikSCAT.

Conventional-resolution DIB and enhanced-resolution AVE and SIR backscatter image products from past and present scatterometer instruments spanning from 1978 to the present are available for download from the SCP project at `www.scp.byu.edu`. To deal with the temporal change, short (1 to 4 day) imaging periods are available. A database of scatterometer-derived Antarctic iceberg positions is also available from the SCP.

Acknowledgment

The author is grateful to the anonymous reviewers for the comments and suggestions, which have benefited this paper.

References

[1] M. W. Spencer, C. Wu, and D. G. Long, "Improved resolution backscatter measurements with the SeaWinds pencil-beam scatterometer," *IEEE Trans. Geosci. Remote Sens.*, vol. 38, no. 1, pp. 89–104, Jan. 2000, doi:10.1109/36.823904.

[2] F. Ulaby and D. G. Long, *Microwave Radar and Radiometric Remote Sensing*. Ann Arbor, MI, USA: Univ. Michigan Press, 2014.

[3] D. G. Long and M. R. Drinkwater, "Azimuth variation in microwave scatterometer and radiometer data over Antarctica," *IEEE Trans. Geosci. Remote Sens.*, vol. 38, no. 4, pp. 1857–1870, Jul. 2000, doi:10.1109/36.851769.

[4] A. P. Paget and D. G. Long, "RapidScat diurnal cycles over land," *IEEE Trans. Geosci. Remote Sens.*, vol. 54, no. 6, pp. 3336–3344, Jun. 2016, doi:10.1109/TGRS.2016.2544835.

[5] Q. P. Remund and D. G. Long, "A decade of QuikSCAT scatterometer sea ice extent data," *IEEE Trans. Geosci. Remote Sens.*, vol. 52. no. 7, pp. 4281–4290, Jul. 2014, doi:10.1109/TGRS.2013.2281056.

[6] L. Wang, M. Sharp, B. Rivard, and K. Steffen, "Melt season duration and ice layer formation on the Greenland Ice Sheet, 2000–2004," *J. Geophys. Res.*, vol. 112, no. F4, 2007, Art. no. F04013, doi:10.1029/2007JF000760.

[7] K. M. Stuart and D. G. Long, "Tracking large tabular icebergs using the SeaWinds Ku-band microwave scatterometer," *Deep-Sea Res. II*, vol. 58, pp. 1285–1300, 2011, doi:10.1016/j.dsr2.2010.11.004.

[8] A. M. Swan and D. G. Long, "Multi-year Arctic sea ice classification using QuikSCAT," *IEEE Trans. Geosci. Remote Sens.*, vol. 50, no. 9, pp. 3317–3326, Sep. 2012, doi:10.1109/TGRS.2012.2184123.

[9] D. S. Early and D. G. Long, "Image reconstruction and enhanced resolution imaging from irregular samples," *IEEE Trans. Geosci. Remote Sens.*, vol. 39, no. 2, pp. 291–302, Feb. 2001, doi:10.1109/36.905237.

[10] K. W. Knowles, "Intercomparison of resampling methods for SSMR Pathfinder in EASE-grid," Jul. 2016. [Online]. Available: support.nsidc.org/entries/49195760-Intercomparison-of-Resampling-Methods-for-SMMR-Pathfinder-in-EASE-Grid

[11] D. G. Long and M. J. Brodzik, "Optimum image formation for spaceborne microwave radiometer products," *IEEE Trans. Geosci. Remote Sens.*, vol. 54, no. 5, pp. 2763–2779, May 2016, doi:10.1109/TGARS.2015.2505677.

[12] R. Lindsley and D. G. Long, "Enhanced-resolution reconstruction of ASCAT backscatter measurements," *IEEE Trans. Geosci. Remote Sens.*, vol. 54, no. 5, pp. 2589–2601, May 2016, doi:10.1109/TGARS.2015.2503762.

[13] D. G. Long and D. L. Daum, "Spatial resolution enhancement of SSM/I data," *IEEE Trans. Geosci. Remote Sens.*, vol. 36, no. 2, pp. 407–417, Mar. 1998.

[14] *QuikSCAT Science Data Product Users's Manual*, Jet Propulsion Laboratory, Pasadena, CA, USA, Document D-18053, 2001.

[15] N. M. Madsen and D. G. Long, "Calibration and validation of the RapidScat scatterometer using tropical rainforests," *IEEE Trans. Geosci. Remote Sens.*, vol. 54, no. 5, pp. 2846–2854, May 2016, doi:10.1109/TGRS.2015.2506463.

[16] R. Kumar, A. Chakraborty, A. Parekh, R. Sikhakolli, B. S. Gohil, and A. S. Kiran Kumar, "Evaluation of Oceansat-2-derived ocean surface winds using observations from global buoys and other scatterometers," *IEEE Trans. Geosci. Remote Sens.*, vol. 51, no. 5, pp. 2571–2576, May 2013, doi:10.1109/TGRS.2012.2214785.

[17] J. P. Bradley and D. G. Long, "Estimation of the OSCAT spatial response function using island targets," *IEEE Trans. Geosci. Remote Sens.*, vol. 52, no. 4, pp. 1924–1934, Apr. 2014, doi:10.1109/TGRS.2013.2256429.

[18] K. Padia, "Oceansat-2 Scatterometer algorithms for sigma-0, processing and products format," Adv. Image Process. Group, Signal Image Process. Area, Space Appl. Centre, Ahmedabad, India, Apr. 2010.

[19] D. G. Long, P. Hardin, and P. Whiting, "Resolution enhancement of spaceborne scatterometer data," *IEEE Trans. Geosci. Remote Sens.*, vol. 31, no. 3, pp. 700–715, May 1993, doi:10.1109/36.225536.

[20] I. S. Ashcraft and D. G. Long, "The spatial response function of SeaWinds backscatter measurements," *Proc. SPIE*, vol. 5151, pp. 609–618, Aug. 2003, doi:10.1117/12.506291.

[21] D. G. Long and R. O. W. Franz, "Band-limited signal reconstruction from irregular samples with variable apertures," *IEEE Trans. Geosci. Remote Sens.*, vol. 54, no. 4, pp. 2424–2436, Apr. 2016, doi:10.1109/TGARS.2015.2501366.

[22] B. A. Williams and D. G. Long, "Reconstruction from aperture-filtered samples with application to scatterometer image reconstruction," *IEEE Trans. Geosci. Remote Sens.*, vol. 49, no. 5, pp. 1663–1676, May 2011, doi:10.1109/TGRS.2010.2086063.

[23] B. A. Williams, "A fieldwise retrieval approach to the noise versus resolution tradeoff in wind scatterometery," *IEEE Trans. Geosci. Remote Sens.*, vol. 51, no. 12, pp. 5259–52722, Dec. 2013, doi:10.1109/TGRS.2012.2233481.

[24] F. Naderi, M. H. Freilich, and D. G. Long, "Spaceborne radar measurement of wind velocity over the ocean—An overview of the NSCAT Scatterometer system," *Proc. IEEE*, vol. 79, no. 6, pp. 850–866, Jun. 1991, doi:10.1109/5.90163.

[25] I. S. Ashcraft and D. G. Long, "Relating microwave backscatter azimuth modulation to surface properties of the Greenland ice sheet," *J. Glaciol.*, vol. 52, no. 177, pp. 257–266, 2006.

[26] R. D. Lindsley and D. G. Long, "ASCAT and QuikSCAT azimuth modulation of backscatter over East Antarctica," *IEEE Geosci. Remote Sens. Lett.*, vol. 13, no. 8, pp. 1134–1138, Aug. 2016, doi:10.1109/LGRS.2016.2572101.

[27] A. D. Fraser, N. W. Young, and N. Adams, "Comparison of microwave backscatter anisotropy parameterizations of the Antarctic ice sheet using ASCAT," *IEEE Trans. Geosci. Remote Sens.*, vol. 52, no. 3, pp. 1583–1595, Mar. 2014.

[28] J. P. Bradley, "Extending the QuikSCAT data record with the Oceansat-2 scatterometer," Master's thesis, Brigham Young Univ., Provo, UT, USA, 2012.

[29] H. Stephen and D. G. Long, "Microwave backscatter modeling of erg surfaces in the Sahara Desert," *IEEE Trans. Geosci. Remote Sens.*, vol. 43, no. 2, pp. 238–247, Feb. 2005, doi:10.1109/TGRS.2004.840646.

[30] K. R. Moon and D. G. Long, "Considerations for Ku-band scatterometer calibration using the dry snow zone of the Greenland ice sheet," *IEEE Geosci. Remote Sens. Lett.*, vol. 10, no. 6, pp. 1344–1349, Nov. 2013, doi:10.1109/LGRS.2013.2241012.

[31] L. Wang, M. J. Sharp, B. Rivard, S. Marshall, and D. Burgess, "Melt season duration on Canadian Arctic Ice Caps, 2000–2004," *Geophys. Res. Lett.*, vol. 32, no. 19, 2005, Art. no. L19502, doi:10.029/2005GL023962.

[32] L. B. Kunz and D. G. Long, "Melt detection in Antarctic ice-shelves using spaceborne scatterometers and radiometers," *IEEE Trans. Geosci. Remote Sens.*, vol. 44, no. 9, pp. 2461–2469, Sep. 2006, doi:10.1109/TGRS.2006.874138.

[33] S. E. L. Howell, A. Tivy, J. J. Yackel, and R. K. Scharien, "Application of a SeaWinds/QuikSCAT sea ice melt algorithm for assessing melt dynamics in the Canadian Arctic Archipelago," *J. Geophys. Res.*, vol. 111, no. C7, 2006, Art. no. C07025, doi:10.1029/2005JC003193.

[34] S. E. L. Howell, J. Assini, K. L. Young, A. Abnizova, and C. Derksen, "Snowmelt variability in Polar Bear Pass, Nunavut, Canada, from QuikSCAT: 2000–2009," *Hydrological Process.*, vol. 26, no. 23, pp. 2477–3488, 2012, doi:10.1002/hyp.8365.

[35] R. Brown, C. Derksen, and L. Wang, "Assessment of spring snow cover duration variability over Northern Canada from satellite dataset," *Remote Sens. Environ.*, vol. 111, pp. 367–381, 2007.

[36] K. Gröchenig, "Reconstruction algorithms in irregular sampling," *Math. Comput.*, vol. 59, no. 199, pp. 181–194, 1992.

[37] K. Gröchenig, "A discrete theory of irregular sampling," *Linear Algebra Appl.*, vol. 193, pp. 129–150, 1993.

[38] Oct. 2016. [Online]. Available: http://en.wikipedia.org/wiki/Geometric_mean

[39] I. Pitas and A. Venetsanopoulos, "Nonlinear mean filters in image processing," *IEEE Trans. Acoust., Speech, Signal Process.*, vol. ASSP-34, no. 3, pp. 573–584, Jun. 1986, doi:10.1109/TASSP.1986.1164857.

[40] P. K. Yoho and D. G. Long, "Correlation and covariance of satellite scatterometer measurements," *IEEE Trans. Geosci. Remote Sens.*, vol. 42, no. 6, pp. 1176–1187, Jun. 2004, doi:10.1109/TGRS.2004.825588.

[41] J. Vogelzang and A. Stoffelen, "ASCAT ultra-high resolution wind products on optimized grids," *IEEE Select. Topics Appl. Earth Observ. Remote Sens.*, vol. 10, no. 3, doi:10.1109/JSTARS.2016.262861.

[42] M. P. Owen and D. G. Long, "Simultaneous wind and rain estimation for QuikSCAT at ultra-high resolution," *IEEE Trans. Geosci. Remote Sens.*, vol. 49, no. 6, pp. 1865–1878, Jun. 2011, doi:10.1109/TGRS.2010.2102361.

[43] A. M. Plagge, D. C. Vandemark, and D. G. Long, "Coastal validation of ultra-high resolution wind vector retrieval from QuikSCAT in the Gulf of Maine," *IEEE Geosci. Remote Sens. Letters*, vol. 6, no. 3, pp. 413–417, Jul. 2009, doi:10.1109/LGRS.2009.2014852.

[44] S. V. Nghiem *et al.*, "Observations of urban and suburban environments with global satellite scatterometer data," *ISPRS J. Photogramm. Remote Sens.*, vol. 64, pp. 367–380, 2009.

[45] D. G. Long, M. W. Spencer, and E. G. Njoku, "Spatial resolution and processing tradeoffs for HYDROS: Application of reconstruction and resolution enhancement techniques," *IEEE Trans. Geosci. Remote Sens.*, vol. 43, no. 1, pp. 3–12, Jan. 2005, doi:10.1109/TGRS.2004.838385.

David G. Long (S'80–SM'98–F'08) received the Ph.D. degree in electrical engineering from the University of Southern California, Los Angeles, CA, USA, in 1989.

From 1983 to 1990, he worked for NASA's Jet Propulsion Laboratory (JPL), where he developed advanced radar remote sensing systems. While at JPL, he was the Project Engineer on the NASA Scatterometer project, which flew from 1996 to 1997. He also managed the SCANSCAT project, the precursor to SeaWinds, which was flown in 1999 on QuikSCAT, in 2002 on ADEOS-II, and in 2014 on the International Space Station. He is currently a Professor in the Electrical and Computer Engineering Department, Brigham Young University, Provo, UT, USA, where he teaches upper division and graduate courses in communications, microwave remote sensing, radar, and signal processing and is the Director of the BYU Center for Remote Sensing. He is the Principle Investigator on several NASA-sponsored research projects in remote sensing. He has more than 400 publications in various areas including signal processing, radar scatterometry, and synthetic aperture radar. His research interests include microwave remote sensing, radar theory, space-based sensing, estimation theory, and signal processing.

Dr. Long received the NASA Certificate of Recognition several times and is an Associate Editor of IEEE GEOSCIENCE AND REMOTE SENSING LETTERS.